Computer Methods and Programs in Biomedicine 270 (2025) 108931

Contents lists available at ScienceDirect

Computer Methods and Programs in Biomedicine

journal homepage: https://www.sciencedirect.com/journal/computer-methods-and-programs-in-biomedicine

In-silico patient-specific modelling of prostate cancer: Predicting PSA dynamics and treatment response

Ángela Pérez-Benito [a], Adrián Galiana-Bordera [b], Pedro-Miguel Martínez-Gironés [b], Gemma Urbanos [c], Anna Nogué Infante [c], María José Gómez-Benito [a], María Ángeles Pérez [a,*]

[a] Multiscale in Mechanical and Biological Engineering (M2BE), Aragon Institute of Engineering Research (I3A), University of Zaragoza, Zaragoza, Spain
[b] Biomedical Imaging Research Group (GIBI230), La Fe Health Research Institute (IIS La Fe), Avenida Fernando Abril Martorell, València, 46026, Spain
[c] Quantitative Imaging Biomarkers in Medicine, Quibim SL, Valencia, Spain

ARTICLE INFO

Keywords:
PCa
PSA dynamics
Treatments
Computational modelling
Personalised medicine

ABSTRACT

Background and Objective: Prostate cancer remains a significant global health concern, with treatment response varying among patients. Radiotherapy, often combined with hormone therapy, is a key treatment approach, but predicting individual outcomes remains challenging. Computational models have emerged as valuable tools to simulate tumour behaviour and optimise treatment strategies. This study presents a patient-specific computational model designed to predict tumour response by associating Prostate-Specific Antigen (PSA) dynamics with tumour biological behaviour under therapy.

Methods: The model integrates patient-specific clinical data and imaging biomarkers from a retrospective study, including apparent diffusion coefficient values from diffusion-weighted imaging to represent tumour cellularity and perfusion parameters from dynamic contrast-enhanced MRI to characterise vascular properties. Clinical data from five patients undergoing radiotherapy, hormone therapy, or combination therapy are used for model development and validation. Due to the limited availability of patient data, PSA is the only parameter used for calibration and validation. One patient is used for calibration, while six serve for validation. Model performance is evaluated by calculating the mean absolute error (MAE) between simulated and observed PSA values post-treatment. The model also estimates tumour shrinkage, though this cannot be directly validated. To assess predictive capacity, two patients are selected for additional analysis simulating different treatment strategies and their impact on PSA dynamics and tumour shrinkage.

Results: The model successfully replicates PSA trends, with MAE values of 0.1, 0.08, 0.23, 0.14, 0.11 and 0.15 ng/mL and RMSE of 0.18, 0.15, 0.24, 0.18, 0.12 and 0.15 ng/mL for the six validation patients, with Patient C showing the closest correspondence to clinical data (MAE = 0.08). Overall, the MAE ranges from 0.08 ng/mL to 0.23 ng/mL, indicating the model's ability to approximate treatment response. In the two selected patients, simulated treatment variations result in distinct PSA dynamics and estimated tumour shrinkage, highlighting interpatient variability in treatment response.

Conclusions: This computational model provides a predictive framework for assessing prostate cancer treatment response based on patient-specific PSA dynamics and imaging biomarkers. While tumour shrinkage estimates cannot be validated, the model offers insights into treatment-induced PSA fluctuations. The findings support the potential of *in-silico* tools in personalised medicine, aiding clinical decision-making by evaluating different therapeutic strategies. Further validation with larger datasets is necessary for clinical integration.

1. Introduction

Prostate Cancer (PCa) is the most common cancer in men and a major health concern worldwide, with rising incidence and mortality projected in the coming decades. Projections indicate a substantial increase by 2050, with incidence expected to rise by 96.2% and mortality by 136.4% [1], highlighting the urgent need for enhanced research and public health strategies to address this growing burden. When PCa is suspected, tissue biopsy remains the standard of care for diagnosis. Diagnosis involves Prostate-Specific Antigen (PSA) blood tests, imaging techniques like Magnetic Resonance Imaging (MRI), and biopsies [2,3].

Risk assessment for PCa combines multiple diagnostic tools. MRI-based evaluation follows the PIRADS v2.1 protocol [4], which assigns

* Corresponding author.
E-mail address: angeles@unizar.es (M.Á. Pérez).

https://doi.org/10.1016/j.cmpb.2025.108931
Received 14 March 2025; Received in revised form 4 June 2025; Accepted 27 June 2025
Available online 14 July 2025

Acronyms

ADC	Apparent Diffusion Coefficient
ADT	Androgen Deprivation Therapy
AS	Active Surveillance
bpMRI	biparametric MRI
BT	Brachytherapy
DCE	Dynamic Contrast Enhanced
DWI	Diffusion Weighted Imaging
EAU	European Association of Urology
EBRT	External Beam Radiotherapy
FE	Finite Element
GS	Gleason Score
HDR-BT	High-Dose Rate BT
HT	Hormonal Therapy
LQ	linear-quadratic
MAE	Mean Absolute Error
mpMRI	multiparametric MRI
MRI	Magnetic Resonance Imaging
ODEs	Ordinary Differential Equations
PCa	Prostate Cancer
PIRADS v2.1	Prostate Imaging Reporting and Data System version 2.1
PSA	Prostate-Specific Antigen
RMSE	Root Mean Square Error
RT	Radiotherapy
STM	Standard Tofts Model
T2WI	T2-Weighted Imaging

a score from 1 to 5 based on tumour texture, location, and volume [5]. Biopsy samples are assessed using the Gleason Score (GS), which sums the two most prevalent histological patterns, each graded on a 1-to-5 scale reflecting microscopic architecture and cellular characteristics [6]. These factors, along with PSA levels and clinical stage, are used to categorise PCa into low, intermediate, or high-risk groups according to the European Association of Urology (EAU) risk group classification [7–9].

Patients with localised PCa have several treatment options, including Active Surveillance (AS), radical prostatectomy, RT, HT, or combinations of these approaches. The choice of treatment is based on the stage and grade of the cancer, as well as individual patient characteristics and preferences. These treatments target PCa cells, inducing apoptosis and reducing tumour burden. As cancer cells die, the production of PSA decreases significantly. PSA levels serve as the primary biomarker to evaluate treatment efficacy [10,11]. A sustained drop in PSA post-treatment often indicates successful cancer control, with patients with a PSA of 0.2 ng/mL or less having the greatest survival advantage, while rising levels may suggest recurrence or resistance [10].

RT is a central treatment modality for PCa, using ionising radiation to destroy cancer cells. It is generally divided into two main types: External Beam Radiotherapy (EBRT) and Brachytherapy (BT). EBRT involves delivering radiation from an external source to the prostate, usually in fractions. This fractionation strategy spreads the total radiation dose over multiple sessions, maximising the effectiveness of the treatment while minimising damage to surrounding healthy tissue [12]. BT, on the other hand, is an internal form of RT in which radioactive sources are placed directly in or near the prostate tumour. High-Dose Rate BT (HDR-BT) is a specific technique used to treat PCa. It uses needles strategically placed in the prostate to deliver radiation directly to the tumour. HDR-BT is often completed in a single session and requires a minor surgical procedure to place the radioactive sources [13]. When combined with EBRT, HDR-BT offers higher cancer control rates than EBRT alone and should be considered for eligible patients with high- or intermediate-risk disease. HT, also known as Androgen Deprivation Therapy (ADT), is another important treatment for PCa, as male hormones (androgens) promote the growth of both prostate gland and cancer cells [14–16]. It works by reducing the levels of male hormones in the body or blocking their effects on PCa cells. HT is often used alongside RT to increase the effectiveness of the treatment. It is particularly effective in treating advanced or metastatic PCa. In this advanced stage of the disease, it can be used as a standalone treatment, or in combination with other treatments, to improve patient outcomes [17].

In biomedical research, computational models have become essential for studying complex diseases like cancer. These models enable researchers to simulate and analyse biological systems at multiple scales, from molecular interactions to cellular dynamics [18]. Numerous models have been developed to investigate tumour growth dynamics and assess treatment effects, significantly advancing our understanding of cancer biology and therapeutic strategies [2,19–21]. Additionally, they help explore tumour–environment interactions and processes such as angiogenesis [22]. Among the most studied computational models in cancer research are those focusing on RT and HT, given their central role in treatment. RT models simulate the effects of ionising radiation on tumour and healthy tissues, often integrating tumour growth dynamics with radiation biology principles, such as the linear-quadratic (LQ) model, which predicts cell survival based on radiation dose and fractionation schedules [23–26]. HT models, on the other hand, simulate the effects of androgen deprivation on tumour progression, particularly in hormone-sensitive cancers such as PCa. These models explore the interplay between androgen levels, cancer cell proliferation, and resistance mechanisms that may emerge during therapy [27]. In PCa research, a significant focus has been placed on computational models that reproduce and predict PSA dynamics. These models, often based on differential equations, describe the interactions between PSA levels, cancer cell populations, and treatment effects. For instance, models in [28–30] incorporate PSA dynamics with HT treatments to predict tumour response, while [31] explored how PSA dynamics can predict RT outcomes.

The integration of advanced imaging techniques, such as biparametric MRI (bpMRI) or multiparametric MRI (mpMRI), aligns with the principles of *in-silico* medicine, leveraging personalised digital models to enhance disease prevention, diagnosis, and treatment [32]. Parameters derived from these techniques, like the Apparent Diffusion Coefficient (ADC) from Diffusion Weighted Imaging (DWI), which inversely correlates with tissue cellularity [20], and vascularisation metrics from Dynamic Contrast Enhanced (DCE)-MRI using pharmacokinetic models such as the Standard Tofts Model (STM), provide detailed insights into tissue characteristics [33–35]. These imaging data, combined with segmentation methods, allow for the generation of patient-specific anatomical models, which are increasingly leveraged in the development of *in-silico* digital twins for PCa.

Despite these advances, several limitations remain in the current literature, particularly in relation to the integration of spatial modelling, imaging biomarkers, and treatment response. For example, the work by Kronik et al. [36] presents a model of PSA dynamics in response to immunotherapy, incorporating immune–tumour interactions across systemic compartments. However, it does not include spatial tumour modelling or anatomical detail, nor does it utilise imaging-derived parameters. More recently, Lorenzo et al. [37] model PSA evolution under RT using clinical data, yet the approach remains non-spatial and does not integrate imaging or treatment-specific modelling. While Lorenzo et al. [38] introduce a 3D tumour growth model based on T2WI and

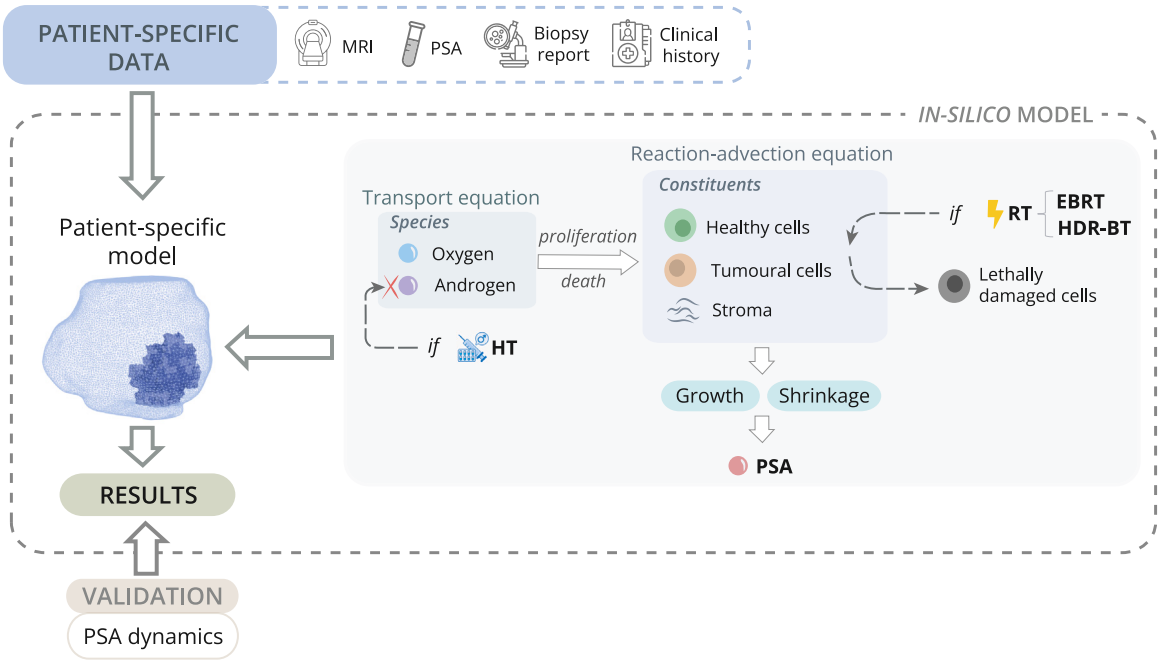

Fig. 1. Overview of the patient-specific model. The patient-specific FE mesh is generated from medical image data (pre-treatment T2WI MRI) and the patient's characteristic data are integrated (cellularity, K^{Trans}, initial PSA, percentage of tumoural cells in biopsy cylinders and clinical history, such as dates when treatments are applied). The model considers multiple constituents (healthy and tumoural cells and stroma), so growth or shrinkage is given by proliferation or death of healthy and tumoural cells and production or degradation of stroma, processes triggered by the presence of species (oxygens and androgens) modelled by the transport equation. All these processes are defined by reaction–advection equations. When HT is applied, the concentration of androgens in the blood decreases and can trigger cell death phenomena. When RT is applied, some cells survive, but others become lethally damaged cells that die at a characteristic time. Finally, PSA is calculated, which reflects the progression of the tumour. The results are subsequently validated with clinical data.

DWI MRI, the model is limited to patients under AS and does not incorporate vascular parameters from DCE-MRI, nor does it simulate therapeutic effects. Moreover, earlier work by the authors focused on AS patients without modelling treatment response or androgen dynamics [39]. A clinically validated, patient-specific framework that combines anatomical geometry, imaging-driven tumour characterisation, and detailed treatment simulation remains unexplored.

The proposed model addresses these gaps by integrating individualised MRI-derived imaging biomarkers within a biomechanical computational framework to represent the prostate and tumour geometry. It incorporates ADC from DWI MRI to characterise tissue cellularity and K^{Trans} from DCE-MRI to characterise vascularisation parameters. A reaction–advection model, solved using the Finite Element (FE) method, captures tumour growth/degrowth and therapeutic effects across space and time. PSA dynamics are explicitly modelled as an indicator of treatment efficacy, and retrospective PSA measurements are used for clinical validation in patients receiving RT, HT, or their combination. This work builds upon the patient-specific computational model developed by Pérez-Benito et al. [39], originally designed for patients under AS, by introducing important advances: (i) simulation of multiple treatment modalities—EBRT, HDR-BT, and HT—each with spatial and temporal specificity, enabling evaluation of single and combined regimens; (ii) introduction of a transported variable to represent androgen concentration, essential for modelling the effects of HT on tumour proliferation and apoptosis; (iii) inclusion of a compartment for lethally damaged cells, improving biological realism by capturing delayed cell death post-RT due to accumulated damage; and (iv) application of the model to intermediate-risk prostate cancer patients undergoing therapy, thereby extending its clinical relevance to a broader patient population. The patient-specific data is taken from a retrospective study.

2. Methods

2.1. Mathematical model

In Pérez-Benito et al. [39] a multi-scale model for PCa growth was presented, focusing on patients with low-risk cancer and whose line of treatment was AS. Here, this model is extended and modified to include new treatment lines, RT and HT, focusing on intermediate-risk patients (Fig. 1).

The prostate is composed of glandular epithelial cells and stroma, with mutations in these cells leading to disrupted glandular structures and increased proliferation. Consequently, the model focuses on three main constituents: healthy cells, tumoural cells, and stroma, each characterised by its density (ρ^i). The dynamics governing the evolution of these population densities are derived from the principles of mass conservation and are described using an advection–reaction equation (Eq. (1)):

$$\begin{aligned}\frac{\partial \rho^i}{\partial t} + \nabla\left(\rho^i \frac{\partial \mathbf{u}}{\partial t}\right) = \\ \rho^i k_g^i \frac{1}{1+\omega^i}\left(\frac{k\rho_c^i - \rho^i}{k\rho_c^i}\right)\mathcal{H}(\rho^o - \theta_p^{i,o})\mathcal{H}(\rho^a - \theta_p^{i,a}) \\ - \rho^i k_d\left[\mathcal{H}(\theta_d^{i,o} - \rho^o) + \mathcal{H}(\theta_d^{i,a} - \rho^a)\right]\end{aligned} \tag{1}$$

where $i = t, h, s$ (t = tumoral cells; h = healthy cells; and s = stroma). The terms on the left side of the equation represent the temporal rate of change of the ith population density and the convective term, while those on the right side correspond to proliferation/production and death/degradation, respectively. The proliferation/production term depends on: k_g^i, the proliferation/production rate; ρ_c^i, the tissue carrying capacity; k, the corrected carrying capacity that limits unlimited cell proliferation and stroma production; and ω^i, a cell-dependent parameter equal to 1 for healthy cells and stroma and 0 for tumoural cells. The

proliferation/production variable rate k_g^i is applied uniformly across all constituents, such that $k_g^h = k_g^t = k_g^s = k_{g,0}$, at least before RT or after a characteristic time, where k_g^i can be affected (see Section 2.1.4). This parameter is modulated by ω^i, which reduces the proliferation/production rate in healthy tissue. The death/degradation process is governed by the constant k_d. Both proliferation/production and death/degradation processes are regulated by oxygen (ρ^o) and androgen (ρ^a) concentrations through Heaviside function $\mathcal{H}$. The thresholds $\theta_p^{i,o}$ and $\theta_d^{i,o}$ denote the oxygen concentration levels required for proliferation/production and death/degradation of constituent i, respectively, while $\theta_p^{i,a}$ and $\theta_d^{i,a}$ denote the corresponding androgen thresholds. Proliferation/production occurs only when sufficient concentrations of both oxygen and androgens are present (multiplicative), whereas death/degradation can result from hypoxia and/or insufficient androgen levels (additive). The k parameter imposes a limit on spatial saturation, ensuring that ρ^i/ρ_c^i never exceeds 1. Additionally, it maintains the necessary space for stroma, thereby preventing excessive cellular proliferation, which is essential for cell survival. The species displacement, $\mathbf{u}(\mathbf{x}, t)$, results from both tumour growth and its deformation as it interacts with the surrounding tissues and organs at position $\mathbf{x}$ and time t.

Oxygen and androgens are transported throughout the prostate and have a significant impact on cell dynamics. Their concentrations are primarily regulated by exchange with the blood, which is directly influenced by prostate vascularisation. This vascularisation is represented by K^{Trans}, derived from DCE-MRI [33], alongside a negative term that accounts for cellular consumption. The transport equation is defined as (Eq. (2)):

$$\frac{\partial \rho^j}{\partial t} + \nabla\left(\rho^j \frac{\partial \mathbf{u}}{\partial t}\right) = K^{Trans}(\rho_b^j - \rho^j) - \sum_i^{h,t} \frac{A^j \rho^j}{k^j + \rho^j} \frac{\rho^i}{\rho_c^i} \tag{2}$$

where $j = o, a$ are the two species (o = oxygen; a = androgens) and $i = t, h$. K^{Trans} represents the extravasation parameter, which defines the supply rate, while ρ_b^j denotes the concentration of the species in the blood. ρ_b^o represents the oxygen concentration in the blood and is assumed to be constant. In contrast, ρ_b^a denotes the concentration of androgens in the blood, which remains constant under physiological conditions. However, when HT is administered, its concentration fluctuates. The coefficients A^j and k^j characterise the species consumption by different constituents of the model. Specifically, A^j is the maximum consumption rate of the species, and k^j represents the species concentration at which the total consumption rate reaches half of its maximum value.

In the model, elevated PSA levels in the tissue are attributed to lumen disruption and leakage caused by tumoural cells [40]. The increase in tissue PSA is assumed to be proportional to the concentration of tumoural cells. Additionally, it is hypothesised that lethally damaged cells do not contribute to PSA production. PSA transfer from tissue to blood (intravasation) is influenced by prostate vascularisation, with K^{Trans} serving as the key physical property driving this exchange. This process depends on the concentration gradient between PSA in the tissue and PSA in the bloodstream. The dynamics of tissue PSA (P) and serum PSA in blood (P_s) are described by Eqs. (3) and (4), respectively:

$$\frac{\partial P}{\partial t} = \lambda^t \frac{\rho^t}{\rho_c^t} - K^{Trans}(P - P_s) - \gamma P \tag{3}$$

$$\frac{dP_s}{dt} = \int \widetilde{K}^{Trans}(P - P_s) dv - \gamma_s P_s \tag{4}$$

where λ^t represents the production rate of PSA by tumoural cells, while γ and γ_s are the natural decay parameters of PSA in the tissue and blood, respectively. Serum PSA in the bloodstream is calculated as the cumulative exchange between tissue and blood across all infinitesimal prostate volumes (dv). The parameter $\widetilde{K}^{Trans}$ denotes the extravasation rate per unit volume.

2.1.1. Response to HT

Prostate tumoural cells are known to be stimulated by androgens [14,16,41], which are male sex hormones secreted mainly by the testes and adrenal glands. Androgens circulate in the bloodstream and enter the prostate tissue, promoting tumour growth. HT aims to reduce androgen levels to inhibit the proliferation of tumoural cells. As a first approximation, the concentration of androgens in the blood (ρ_b^a) is modelled as varying with the activation of the treatment. When the treatment is inactive, the androgen concentration remains at a constant basal level ($\rho_{b,0}^a$) derived from the literature. However, when the treatment is active, this concentration is set to zero, simulating the effect of the drugs on the testes and adrenal glands. After treatment is completed, hormone levels in bloods does not recover instantly, but need a characteristic time to recover [42]. Androgen blood dynamics is described by Eq. (5):

$$\rho_b^a = \begin{cases} \rho_{b,0}^a, & \text{if } t < t_{HT}, \\ \rho_{b,0}^a \left(1 - \exp\left(-\frac{t - t_{HT}}{\tau_{r,HT}}\right)\right), & \text{if } t \geq t_{HT}. \end{cases} \tag{5}$$

where $\tau_{r,HT}$ is the characteristic time for androgen levels to recover and t_{HT} comprises the time during which the HT is applied.

2.1.2. Survival fraction for EBRT

The LQ model is one of the key tools in radiation biology and physics, widely employed to analyse and predict cellular responses to ionising radiation in both *in-vitro* and *in-vivo* studies [43]. It provides a simple relationship between cell survival and delivered dose. The most common formulation of the LQ model describes the SF of a cell after exposure to a single dose of radiation as expressed in Eq. (6):

$$SF = \exp\left(-\alpha D - \beta D^2\right) \tag{6}$$

where α and β are parameters describing the cell's radiosensitivity (the linear and the quadratic component of cell killing, respectively), and D is the dose to which it is exposed.

If cells are allowed sufficient time to recover after irradiation (on the order of 6–24 h), sub-lethal damage from the initial exposure will be fully repaired, and cells will respond as if they had not previously been irradiated. This principle underlies EBRT, where the total dose is delivered in well-separated fractions of low doses. For exposure to n fractions of dose d, the predicted survival is given by Eq. (7):

$$SF = \left(\exp\left(-\alpha d - \beta d^2\right)\right)^n = \exp\left(-n(\alpha d + \beta d^2)\right) = \exp\left(-D(\alpha + \beta d)\right) \tag{7}$$

where D is again the total exposure dose, given by $D = nd$.

2.1.3. Survival fraction for BT

The standard LQ model has known limitations, particularly in accurately describing clonogenic cell survival curves at high doses. To address these shortcomings, modifications to the LQ model have been proposed, specifically for high-dose-per-fraction regimens [44–46]. Since brachytherapy involves high-dose treatments, the linear–quadratic–linear (LQ–L) model is applied in this context [47]. This model aligns with the behaviour of the LQ model below a transition dose (D_T) and transitions to a linear response above this threshold (Eq. (8)).

$$SF = \begin{cases} \exp\left(-(\alpha D + \beta D^2)\right) & \text{if } D < D_T \\ \exp\left(-(\alpha D_T + \beta D_T^2 + \mu(D - D_T))\right) & \text{if } D \geq D_T \end{cases} \tag{8}$$

where the transition dose is given by $D_T = \frac{2\alpha}{\beta}$. In the high-dose region, the cell kill per Gy (1 Gy = 1 Gray = 1 Joule/kg) in the final linear portion of the survival curve is represented by μ, defined as $\mu = \alpha + 2\beta D_T$.

2.1.4. Response to radiation

The population density of the tissue constituents ρ^i, governed by Eq. (1), is modified during radiation events that occur at times $t_1, t_2, \dots, t_k$. Each irradiation event results in a fraction of cells, known as the survival fraction (SF), capable of repairing radiation-induced damage. Conversely, the remaining fraction, $(1 - SF)$, represents cells that sustain irreparable damage (ρ_d^i). SF are defined in Sections 2.1.2 and 2.1.3 according to the type of radiation applied. These lethally damaged cells transition to a separate compartment. Therefore, following each irradiation event, the population densities (ρ^i) remain as Eq. (9) and Eq. (10):

$$\rho^i(t_k^+) = \rho^i(t_k^-)SF^i \tag{9}$$

$$\rho_d^i(t_k^+) = \rho_d^i(t_k^-) + \rho^i(t_k^-)[1 - SF^i] \tag{10}$$

where $\rho^i(t_k^+)$ means the density right after the radiation event and $\rho^i(t_k^-)$ means the density right before. Initially, ρ_d^i is 0 until the first radiation event, occurring at time t_1. A key aspect of the cell response to radiation is that irradiated cells usually die because of the so-called mitotic catastrophe after completing one or several mitoses [48], thus it is considered that after a characteristic time τ_d these cells die, following an exponential decay. Therefore, the subsequent evolution of the lethally damaged cells (ρ_d^i) follow Eq. (11):

$$\frac{\partial \rho_d^i}{\partial t} = \rho^i(1 - SF^i)\delta(t - t_k) - \sum_k \rho^i(t_k)\left(1 - SF^i\right)\exp\left(-\frac{t - t_k}{\tau_d}\right) \tag{11}$$

During treatment, radiosensitive tumoural cells decrease their rate of cell proliferation through cell cycle arrest stimulated by DNA damage. Then, DNA repair mechanisms are activated to alleviate damage, but cell death mechanisms are activated if damage persists and cannot be repaired. Interestingly, some cells can avoid apoptosis because genome damage triggers cellular overactivation of some DNA repair pathways [49]. RT often induces a temporary decrease in cell proliferation due to damage and cell cycle arrest. This is described in Eq. (12).

$$k_g^i = \begin{cases} k_{g,0}, & \text{if } t < t_k, \\ k_{g,0}\left(1 - \exp\left(-\frac{t - t_k}{\tau_{r,RT}}\right)\right), & \text{if } t \geq t_k. \end{cases} \tag{12}$$

where k_g^i is the proliferation variable rate, $\tau_{r,RT}$ is the characteristic time of cell repopulation [25] and t_k is again any instant when RT is applied. After RT, cells initially recover slowly (dominated by sublethal damage repair and cell cycle arrest), and as time progresses, recovery accelerates and approaches a plateau (full recovery) [50].

2.2. Implementation

The proposed model was implemented in FE to simulate tumour and prostate growth based on patient-specific MRIs. Following the model in [39], biological and mechanical analyses are decoupled, with tumour growth programmed in Python and elastic deformation calculated in Ansys® Academic Research Mechanical using thermoelastic expansion equations as an analogy to growth equations [19,51]. The growth kinematics involving the tumour and prostate are explained in detail in [39]. Prostate domain is modelled by assuming that cells and the stroma contribute to total stress under finite strain assumption, with equal strain in both components. Both cells and stroma are assumed linear elastic isotropic material. Their elastic moduli and Poisson ratio are listed in Table 2.

To do so, the tumour domain is discretised in two overlapping conforming meshes sharing the nodes of the elements, one for the cells and the other for the stroma. Time-integration of the biological solver module is achieved using an explicit numerical scheme (forward Euler method), whereas the growth solver uses a full-implicit iterative scheme (Newton–Raphson). The prostate volume is discretised into a 3D tetrahedral mesh with an element size of 2.5 mm, as this provides a good compromise between computational efficiency and accuracy. Table 1 summarises the number of nodes and elements of the FE mesh for each patient.

Table 1
Number of nodes and elements for each patient.

Patient	Number nodes	Number elements
PATIENT A	2272	9780
PATIENT B	4304	20,156
PATIENT C	3105	14,295
PATIENT D	3026	13,857
PATIENT E	3029	13,651
PATIENT F	5765	28,260
PATIENT G	2535	11,500

As detailed in previous work [39], a multiscale temporal algorithm is employed to integrate cellular processes like proliferation and death (time step of 10 days) with faster phenomena such as species transport and PSA leakage. For species transport, equilibrium is assumed to be reached within a small interval (Δt_d) before each simulation step (Δt). Cellular processes are then updated using an 8th-order explicit Runge–Kutta method for Ordinary Differential Equations (ODEs).

Similarly, PSA dynamics assume rapid equilibrium between tissue and blood concentrations within Δt. The total PSA produced or decayed (P^*) is estimated (Eq. (13)), and equilibrium serum PSA levels are calculated to determine the corresponding tissue concentration (Eq. (14) and Eq. (15)). These steps simplify computation using the explicit Euler method for ODEs.

$$\frac{\Delta P^*}{\Delta t} = \lambda^t \frac{\rho^t}{\rho_c^t} - \gamma P \tag{13}$$

$$\frac{\Delta P_s}{\Delta t} = \sum K^{Trans}(P^* - P_s) - \gamma_s P_s = 0 \tag{14}$$

$$\frac{\Delta P}{\Delta t} = \lambda^t \frac{\rho^t}{\rho_c^t} - K^{Trans}(P - P_s) - \gamma P = 0 \tag{15}$$

The prostate is situated within a region defined by neighbouring organs, primarily the rectum and bladder. These organs undergo natural daily variations due to their physiological activities, which alter their physical properties and make it difficult to determine a material stiffness that accurately reflects the surrounding anatomy. To simplify this complexity, the mechanical properties of these organs are often approximated using an elastic model [60,61]. In this approach, to replicate the stiffness of the surrounding tissues, a distributed elastic foundation ($K_{stiffness}$) is applied as boundary conditions in the direction normal to the prostate.

The parameters employed in this study were initially calibrated and validated in our previous work Pérez-Benito et al. [39], and are summarised in Table 2. This earlier study focused on modelling tumour evolution during AS, and involved an optimisation procedure to estimate key parameters, ensuring the biological realism and clinical relevance of the model. The Supplementary Material provides the results of a global sensitivity analysis of the parameters of the model based on the Morris screening method. In the present work, these parameters are adopted as a foundation, extending the model to include treatment dynamics and additional biological processes. To fit the model, some parameters from the PSA dynamics equations are optimised. The parameters related to RT and HT have been collected in Tables 3 and 4 and have been extracted from bibliography. This work focuses primarily on the tumour response to treatments. As a first approximation, it is assumed that the treatments do not directly affect the healthy cell populations. This assumption is based on two factors: firstly, healthy cells are not as sensitive to androgen fluctuations as tumoural cells; secondly, the planning of both EBRT and HDR-BT schemes explicitly takes into account the recovery times of healthy cells in order to minimise collateral damage.

Table 2
Parameters of the model.

Symbol	Parameter	Value	Units	References
$k_{g,0}$	Proliferation rate	$4.03 \cdot 10^{-3}$	day^{-1}	[39]
k	Carrying capacity corrected	0.57	–	[39]
ρ_c^t	Tissue tumour cell carrying capacity	$100 \cdot 10^3$	cells mm^{-3}	[20]
ρ_c^h	Tissue healthy cell carrying capacity	$75 \cdot 10^3$	cells mm^{-3}	[20]
ρ_c^s	Tissue stroma carrying capacity	1.50	g mm^{-3}	[52]
k_d	Death rate	0.02	day^{-1}	[2]
$\theta_p^{t,o}$	Proliferation oxygen threshold (tumoral cells)	3500	pmol	[53]
$\theta_d^{t,o}$	Necrosis oxygen threshold (tumoral cells)	3000	pmol	[53,54]
$\theta_p^{h,o}$	Proliferation oxygen threshold (healthy cells)	4000	pmol	[53]
$\theta_d^{h,o}$	Necrosis oxygen threshold (healthy cells)	3300	pmol	[53,54]
$\theta_p^{s,o}$	Oxygen threshold for stroma production	4000	pmol	[53]
$\theta_d^{s,o}$	Necrosis oxygen threshold (stroma)	3900	pmol	[53,54]
A^o	Maximum oxygen consumption rate	25.50	pmol s^{-1}	[55]
k^o	Oxygen concentration at one-half of the total consumption term	4.64	pmol	[55]
ρ_b^o	Oxygen blood concentration	4124	pmol	[55]
$K_{stiffness}$	Stiffness of prostate surroundings	14	kPa/mm	[39]
E^t	Young's modulus of tumoral cells	3	kPa	[56,57]
E^h	Young's modulus of healthy cells	5	kPa	[56,57]
E^s	Young's modulus of stroma	30	kPa	[58]
ν	Poisson's ratio	0.40	–	[59]
λ^t	PSA production rate (tumoral cells)	142.55	ng mL^{-1} day^{-1}	Optimised
γ	Tissue PSA decay rate	0.018	day^{-1}	Optimised
γ_s	Blood PSA decay rate	0.25	day^{-1}	[2]

Table 3
HT parameters.

Symbol	Parameter	Value	Units	References
$\rho_{b,0}^a$	Basal androgen concentration in blood	25	nmol	[29,30]
A^a	Maximum androgen consumption rate	0.00127	nmol/s	[29]
k^a	Androgen concentration at one-half of the total consumption term	0.104	nmol	[29]
$\tau_{r,HT}$	Characteristic time of androgens recover in blood	558	days	[42]
$\theta_p^{t,a}$	Proliferation androgen threshold (tumoural cells)	10	nmol	[29]
$\theta_d^{t,a}$	Death androgen threshold (tumoural cells)	0.05	nmol	[29]
$\theta_p^{(h,s),a}$	Proliferation androgen threshold (healthy cells and stroma)	35	nmol	Estimated
$\theta_d^{(h,s),a}$	Death androgen threshold (healthy cells and stroma)	0	nmol	Estimated

Table 4
RT parameters.

Symbol	Parameter	Value	Units	References
α	Radiosensitivity parameter (tumour cells)	0.073	Gy^{-1}	[24]
α/β	α/β ratio (tumour cells)	2.29	Gy	[24]
$\tau_{r,RT}$	Characteristic time of cell repopulation	28	days	[25]
τ_d	Characteristic time of death by radiation	60	days	[62]

2.3. Adjusting PSA parameters

The PSA model parameters for production and tissue decay (λ^t and γ) are determined through an optimisation process due to their model-specific nature and the significant variability reported in existing research. This variability makes the assignment of fixed, universally applicable values challenging. To address this, an optimisation process is performed using the Python library Optuna [63]. Optuna is a robust and widely used hyperparameter optimisation framework that uses advanced techniques to fine-tune machine learning and computational models. Its standard sampler, the Tree-structured Parzen Estimator (TPE), implements a Bayesian optimisation algorithm to efficiently explore the parameter space [63]. This involves running the tumour growth model a number of times, each run being referred to as a 'trial'. During each trial, the parameters (λ^t and γ) are varied within predefined ranges representing the search space. The goal of optimisation is to identify the set of parameter values that minimises a defined loss function.

To do this, clinical PSA data are used. Therefore, the loss function evaluates how well the simulated PSA data matche the real clinical PSA data to capture the dynamics of the PSA behaviour. As PSA data is often insufficient, moreover just before the treatment starts, synthetic pretreatment PSA is generated, assuming PSA levels before treatment follow an exponential growth curve [64,65]. Given the variability of these measurements due to various patient and environmental factors, the Mean Absolute Error (MAE) is selected as the objective function for minimisation (Eq. (16)), owing to its robustness against outliers:

$$\mathrm{MAE} = \frac{1}{N}\sum_{i=1}^{N} \left|\mathrm{PSA}_{\mathrm{sim}} - \mathrm{PSA}_{\mathrm{clin}}\right| \tag{16}$$

where PSA_{sim} is the simulated PSA value, $\mathrm{PSA}_{\mathrm{clin}}$ is the clinical PSA value and N is the number of clinical PSA time points.

To ensure the simulated PSA data reflects an increasing trend before treatment, decreases in the simulated PSA during the pretreatment phase are penalised. The trend penalty is defined as Eq. (17):

$$\mathrm{Penalty}_{\mathrm{trend}} = \left(\frac{1}{N_{\mathrm{pre}} - 1} \sum_{i=1}^{N_{\mathrm{pre}}-1} \min(0, \mathrm{PSA}_{\mathrm{sim}}(t_{i+1}) - \mathrm{PSA}_{\mathrm{sim}}(t_i)) \right)^2 \tag{17}$$

where $\mathrm{PSA}_{\mathrm{sim}}(t_{i+1}) - \mathrm{PSA}_{\mathrm{sim}}(t_i)$ is the difference between consecutive simulated PSA values and N_{pre} is the are the PSA data point pretreatment.

The total loss combines the MAE and the trend penalty:

$$\mathcal{L} = w_{\mathrm{PSA}} \cdot \mathrm{MAE} + w_{\mathrm{pen}} \cdot \mathrm{Penalty}_{\mathrm{trend}} \tag{18}$$

where w_{PSA} and w_{pen} represent the weights for the MAE and penalty terms, set to 1 and 0.5, respectively.

2.4. Integration of patient-specific data

The model presented in this study has been applied to retrospective data from patients diagnosed with prostate cancer at Hospital Universitario y Politécnico de La Fe de Valencia (HULAFE) between 2015 and 2020 as part of the ProCanAid research project (PLEC2021-007709). The study did not influence routine clinical practice.

To be included, patients had to meet specific criteria: they had to be men over 18 years old with a confirmed prostate cancer diagnosis through a positive biopsy, have received treatment at HULAFE, undergone at least one pre-treatment mpMRI scan, had regular PSA blood tests, and possess essential clinical and pathological data such as risk-group stratification, treatment regimen, GS, or biopsy tumour burden. Upon meeting these inclusion criteria, patient data were anonymised, structured, and curated before being integrated into the study and uploaded to the Qp-Insights®(Quibim S.L) project platform.

Patient-specific imaging biomarkers were extracted from mpMRI scans (see Supplementary Material for acquisition details) and analysed using QP-Prostate®(Quibim S.L.) software, a module within Qp-Insights®(Quibim S.L). The software first performed image pre-processing, including spatial smoothing, motion correction, and intra-series registration of dynamic volumes from DWI and DCE sequences. This was followed by inter-series registration of the DWI and DCE sequences to the T2WI sequence. Following pre-processing, key biomarkers were extracted. Prostate segmentation was based on the T2WI sequence, while tumour segmentation utilised a combination of T2WI and DWI sequences. Additionally, the ADC map was obtained from the DWI sequence, while perfusion parameters, such as K^{Trans}, were computed from the DCE sequence using the STM approach [66]. To further ensure consistency, a standardised arterial input function (AIF) is applied during pharmacokinetic modelling to compute K^{Trans}. The ADC quantifies the diffusion magnitude of water molecules within tissue and has been shown to inversely correlate with tissue cellularity. Consequently, cellularity can be estimated using Eq. (19) [20]:

$$cellularity = \frac{ADC_w - ADC(\mathbf{x})}{ADC_w - ADC_{min}} \tag{19}$$

where ADC_w represents the ADC value of free water molecules, with $ADC_w = 3 \cdot 10^{-3}$ mm^2/s [20], $ADC_{\min}$ is the minimum acquired ADC value, set to 0 to ensure consistency of cellularity values across different patients and follow-up MRIs and $ADC(\mathbf{x})$ is the ADC value in each point, $\mathbf{x}$, of the prostate. This formulation inherently normalises cellularity with respect to the patient-specific ADC distribution, helping to reduce sensitivity to inter-patient acquisition variability.

The K^{Trans} parameter is obtained from the DCE sequence and represents the transfer constant, which quantifies the rate at which the contrast agent moves from blood plasma into the extracellular extravascular space or tumour interstitium [67]. This parameter provides crucial insights into tissue permeability, vessel surface area, and blood flow, making it a valuable indicator of prostate vascularisation [33].

To reconstruct the 3D geometry of the different prostates and generate the volumetric FE mesh required for subsequent simulations, the Python library im2mesh [68] is employed. The values of cellularity and K^{Trans} are then interpolated at the integration points of each mesh element using a nearest-neighbour interpolation method to establish the model's initial parameters. Furthermore, tumour segmentations are used to create a mask that identifies the mesh elements containing tumour cells. Biopsy data provide additional details, such as the GS and tumour burden, which indicate the overall proportion of tumour cells within each sampled cylinder. For patients who have received RT, a radiation dose map (registered in the T2WI sequence) is available, outlining the radiation absorbed by the tissue. These isodose curves are derived from RT treatment planning techniques that utilise medical imaging data. Similar to ADC and K^{Trans}, the absorbed radiation doses are interpolated at the integration points of the mesh elements to define the model's initial conditions.

3. Results

3.1. Application to patient-specific data

The proposed methodology is applied to seven patients diagnosed with PCa, all presenting localised tumours and classified as intermediate-risk by the EAU risk classification. These patients have a GS of (3+4) 7 and a PIRADS v2.1 score between 4 and 5. They have received different combinations of treatment, including EBRT, HDR-BT and HT. All patients received EBRT at some stage of their clinical history; five also underwent HDR-BT three were treated with a combination of HT, EBRT, and HDR-BT and one was treated with a combination EBRT and HT. At the time of diagnosis, these patients underwent mpMRI. From these images, the prostate volume and FE mesh are reconstructed. In addition, image biomarkers, clinical data and tumour location are interpolated to initialise the model. Additional patient-specific details are provided in Fig. 2. Patient A is used to optimise the PSA parameters while the rest six patients are used to validate the model.

3.2. PSA dynamics fitting

Patient A was chosen to undergo the optimisation process. Out of 132 trials, the process successfully identified the optimal parameter combination for accurately fitting the PSA dynamic curve. The best fit was achieved with a minimal loss of 0.7563, corresponding to parameter values of $\lambda^t = 142.55$ ng mL^{-1} day^{-1} and $\gamma = 0.018$ day^{-1}.

Analysing the PSA curve obtained, the MAE post-treatment is of 0.5 ng/mL and the Root Mean Square Error (RMSE) of 0.5 ng/mL, indicating a relatively small deviation from the expected values after the intervention (Fig. 3). The computational analysis of the PSA curve reveals that the PSA half-life (the time required for the PSA level to decrease by half) is approximately 40 days following treatment. According to the estimated computational curve, PSA levels drop below 0.5 ng/mL approximately 180 days after the treatment was administered. Clinically, measurements show that PSA reached a value of 0.2 ng/mL 155 days post-treatment, suggesting a favourable response to the therapy.

Despite the fact that PSA is the only direct data available to optimise or validate the response of tumour volume to treatment, the model provides insight into the expected effects. By the time PSA levels fall below 0.5 ng/mL computationally, the model estimates a 17.6% reduction in tumour volume. The tumour reaches its minimum volume at the end of the simulation, with a final reduction of 30.2% from its initial size. These volume changes highlight the effectiveness of the treatment in reducing the tumour.

3.3. Model prediction after treatment

The presented model is applied to patients B to G to assess whether the predicted PSA values accurately align with those observed in clinical practice. For all six patients, the PSA dynamics exhibit an initial rise prior to treatment, followed by a sharp drop post-treatment and subsequent stabilisation (Fig. 4), closely mirroring clinical observations. Patient C demonstrates the closest correspondence to clinical data (MAE = 0.08). Nonetheless, the MAE for all patients ranges from 0.08 ng/mL to 0.23 ng/mL and the RMSE from 0.15 ng/mL to 0.25 ng/mL, indicating that the simulation effectively predicts clinically observed PSA outcomes.

The time to PSA half-life represents how quickly PSA levels decrease by half, reflecting the tumour's immediate response to therapy. Among the patients, the model estimates that this metric varies from 48 days (Patient E) to 70 days (Patient B), suggesting that Patient E exhibited the fastest reduction in PSA levels, while Patient B showed the slowest initial response (Table 5). Patient E was only treated with EBRT while patient B has undergone a combination of the three modalities of

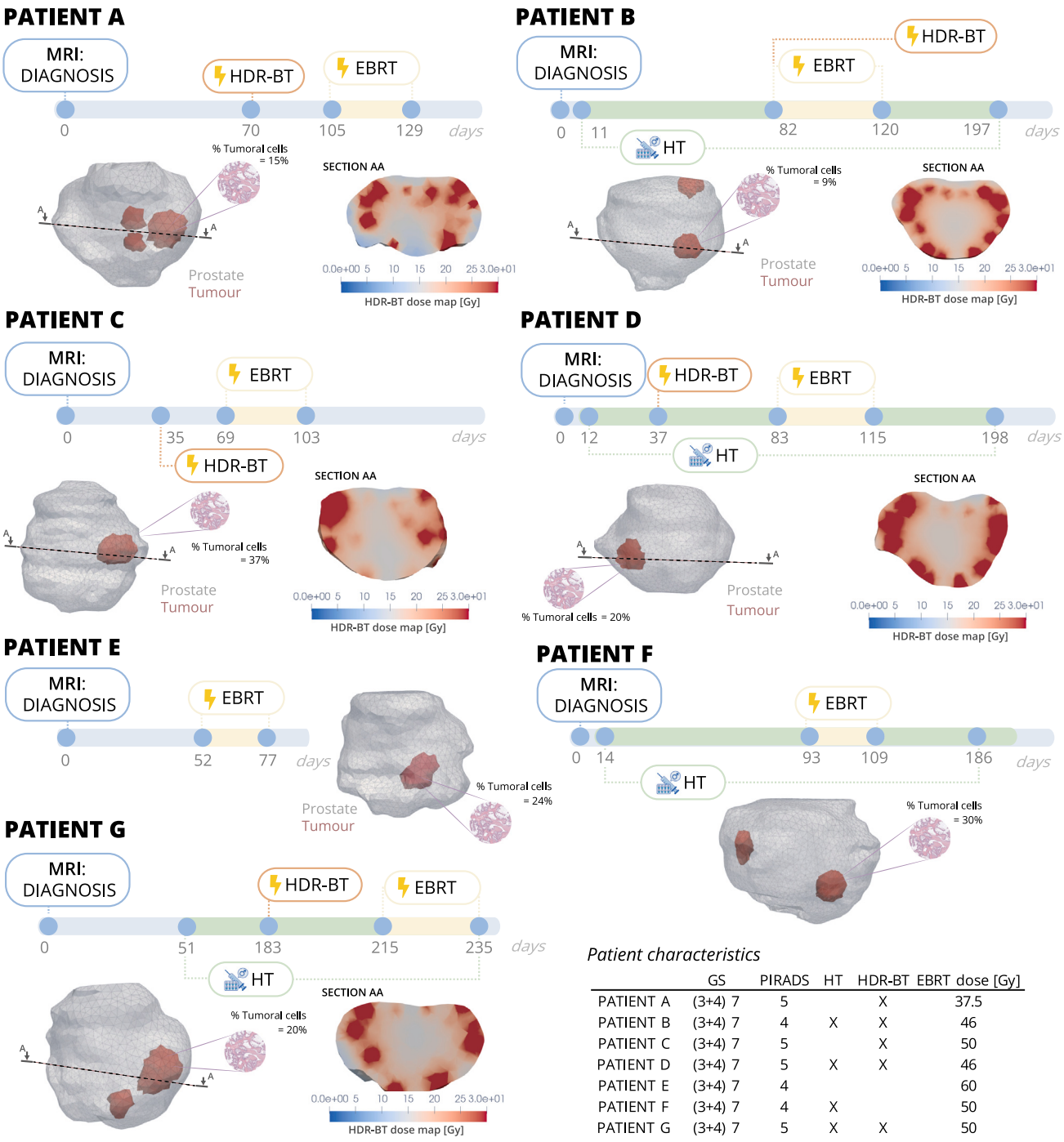

Patient characteristics

	GS	PIRADS	HT	HDR-BT	EBRT dose [Gy]
PATIENT A	(3+4) 7	5		X	37.5
PATIENT B	(3+4) 7	4	X	X	46
PATIENT C	(3+4) 7	5		X	50
PATIENT D	(3+4) 7	5	X	X	46
PATIENT E	(3+4) 7	4			60
PATIENT F	(3+4) 7	4	X		50
PATIENT G	(3+4) 7	5	X	X	50

Fig. 2. Patients clinical history and initial parameters. All patients underwent mpMRI at the time of diagnosis, from which the initial prostate FE mesh was generated. Elements containing tumoural cells are highlighted in red and the total percentage of such cells is given, information extracted from the biopsy reports at the diagnosis time. In addition, for patients who underwent HDR-BT, a mid-section view is provided to illustrate the dose map during treatment. The table illustrates the diagnosis characteristics of each patient (GS and PIRADS v2.1), the treatments that have received and the total dose received of EBRT. Patient E received EBRT exclusively, patients A and C received HDR-BT in addition to EBRT; patients B, D and G received a combination of HT, HDR-BT and EBRT; and patient F received HT and EBRT.

treatments presented. It is also observed that patient G and D, also with EBRT, HDR-BT and HT, have the second and third slowest responses, respectively, followed by patient F, whose line of treatment was EBRT and HT. Therefore, slower treatment responses are predicted in patients who undergo HT.

The time to decay below 0.5 ng/mL represents the total duration required for PSA levels to fall below the clinically significant threshold of 0.5 ng/mL. This metric captures both the initial response and the sustained efficacy of treatment. In this case, the variation predicted is more pronounced, ranging from 166 days (Patient F) to 240 days (Patient B). These values cannot be directly compared with clinical data due to insufficient clinical measurements. However, the first observed clinical values post-treatment were already below 0.5 ng/mL, occurring within 112–266 days after treatment. Despite Patient E demonstrating the fastest PSA half-life, their PSA levels do not fall below 0.5 ng/mL, possibly due to slower PSA clearance following the initial decline. This

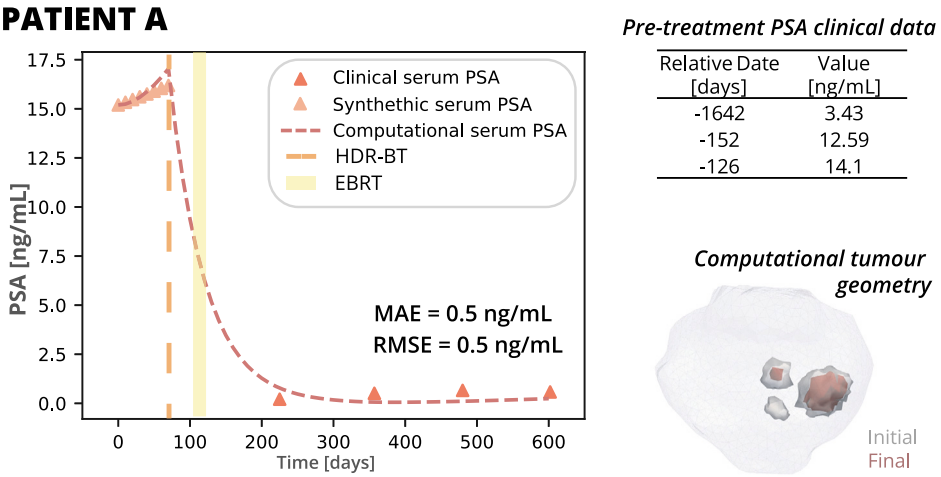

Fig. 3. Simulated PSA curve for patient A after the optimisation process, with parameters $\lambda^I = 142.55$ ng mL^{-1} day^{-1} and $\gamma = 0.018\ day^{-1}$. The adjusted computational serum PSA (red dotted line) compared with clinical PSA data (orange triangles) with the estimated post-treatment MAE and RSME. Synthetic pre-treatment PSA values generated for calibration purposes are shown as light orange triangles. Clinical pre-treatment PSA values are not displayed here, as they are temporally distant from the start of the simulation and would distort the graphical representation. Instead, a table with clinical pre-treatment data is shown. The date is relative to the beginning of the simulation. Treatments are indicated on the graphs: orange dashed lines for HDR-BT and yellow for the duration of EBRT. The 3D representation of the patient's prostate is represented on the right of the image, with the final tumour geometry highlighted in red and the initial configuration in dark grey.

Table 5
Clinical and computational data for tumour response to treatment. The clinical data includes the time after treatment to the first PSA value below 0.5 ng/mL and the corresponding PSA value. The computational forecast includes the time to PSA half-life, the time to decay below 0.5 ng/mL, the percentage of tumour volume shrinkage when PSA is below 0.5 ng/mL, and the maximum percentage volume reduction.

	Clinical data		Computational forecast			
	Time after treatment [days]	First clinical PSA value below 0.5 [ng/mL]	Time to PSA half-life	Time to decay below 0.5 ng/mL	% Volume shrinkage when PSA < 0.5 ng/mL	Maximum % volume shrinkage
PATIENT B	266	0.012	70	240	29.19	37.96
PATIENT C	222	0.003	55	195	10.57	34.76
PATIENT D	266	0.016	58	218	22.21	39.4
PATIENT E	387[a]	0.61[a]	48	315[b]	17.22[b]	28.2
PATIENT F	112	0.09	56	166	24.37	40.44
PATIENT G	246	0.06	69	189	32.28	40.58

[a] Last acquired clinical value did not reach a value below 0.5 ng/mL.
[b] Computational simulations did not reach a value below 0.5 ng/mL; this data corresponds to a PSA of 0.7 ng/mL.

aligns with clinical data, as the most recent PSA measurement, taken 387 days after treatment, showed a value of 0.61 ng/mL.

The observed drop in PSA reflects the death of tumoural cells, which is accompanied by a reduction in tumour volume. Thus, the model primarily estimates the tumour's response to treatment. The tumour volume shrinkage at the time PSA levels fall below 0.5 ng/mL is measured (Table 5). Patients exhibit varying degrees of predicted tumour shrinkage, ranging from 10.57% (Patient C) to 32.28% (Patient G). This indicates that while Patient C achieved a rapid PSA decline, the physical reduction in tumour size was less pronounced compared to others.

Additionally, the maximum percentage of predicted volume reduction during the course of treatment is assessed (Table 5), offering a broader perspective on treatment efficacy. This reduction ranges from 28.2% (Patient E) to 40.58% (Patient G). These findings reveal that although Patient E demonstrated a rapid PSA decline, their overall tumour shrinkage was lower, and their minimum PSA value (0.7 ng/mL) remained higher than that of other patients. Conversely, Patient G, who exhibited a more moderate PSA response, achieved the greatest tumour volume reduction.

Table 6
Analysis of patient B computational results for different treatment strategies. It includes the maximum percentage of tumour volume shrinkage, the time to PSA half-life, the time to decay below a threshold of 0.5 ng/mL and the minimum PSA.

Treatment	Max Shrinkage [%]	PSA Half-Life [days]	Time to Threshold [days]	PSA min [ng/mL]
Control	33.11	52.55	195.09	0.141
HT(3M)+ EBRT+HDR-BT	32.31	52.55	196.83	0.338
EBRT+HDR-BT	35.22	44.94	169.56	0.075
EBRT	33.68	44.94	169.56	0.136
HDR-BT	35.33	44.95	169.71	0.080

3.4. Further analysis

In order to evaluate the effects of different treatment strategies on individual patient responses and show the model predictive capacity,

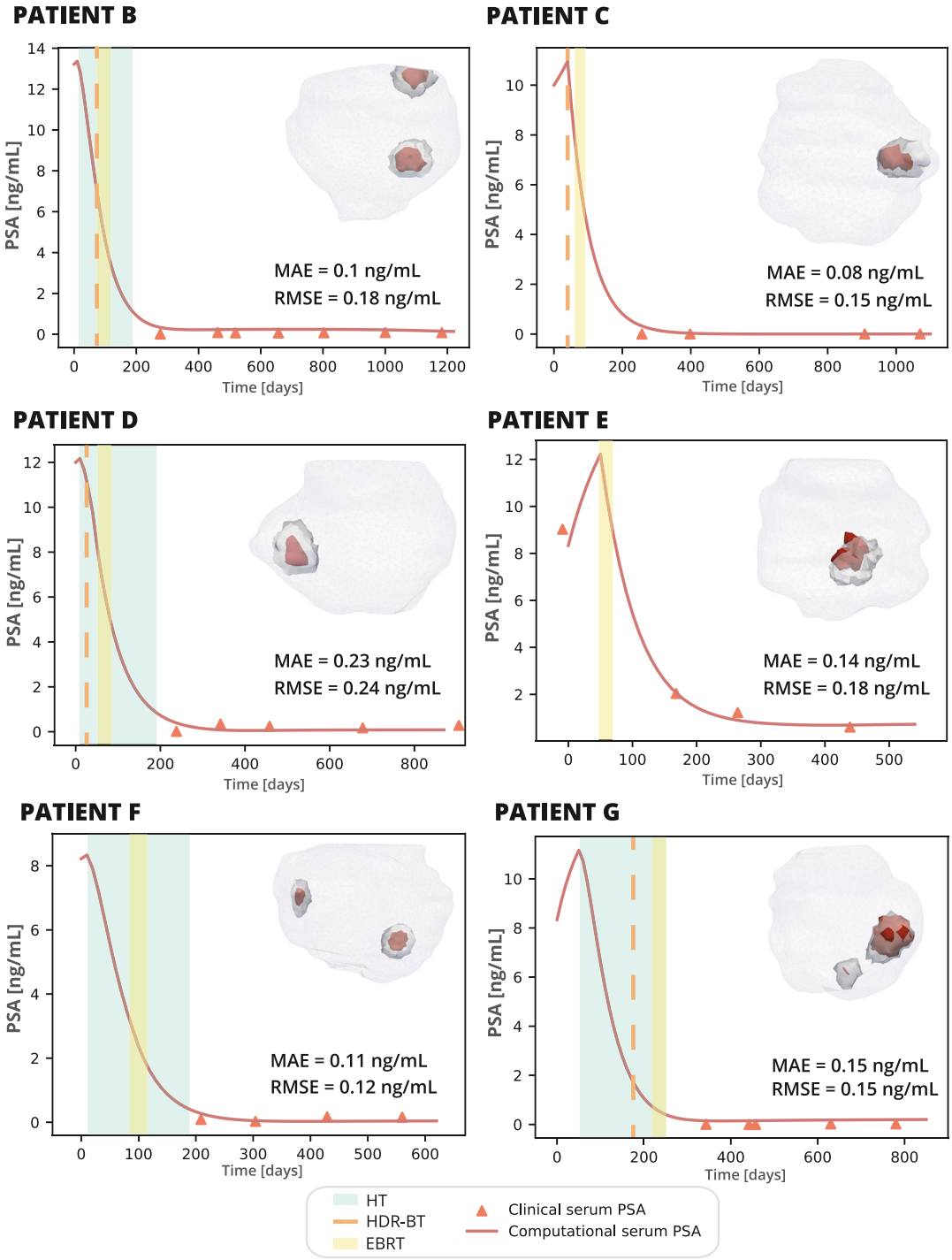

Fig. 4. Computational serum PSA forecasts for the different patients (red line) compared with clinical PSA data (orange triangles). The MAE and RMSE is estimated post-treatment. Treatments are indicated on the graphs: green for the duration of HT, orange dashed lines for HDR-BT, and yellow for the duration of EBRT. The 3D representation of the patient's prostate is represented on the right corner of each patient's graph, with the final tumour geometry highlighted in red and the initial configuration in dark grey.

an additional analysis was conducted using Patients B and C. For Patient B, five treatment variations were examined (Fig. 5 **A**): (i) reducing HT to three months, (ii) omitting HT and proceeding directly with HDR-BT and EBRT, (iii) administering EBRT alone and (iv) using HDR-BT alone. In contrast, Patient C underwent three treatment scenarios (Fig. 6 **A**): (i) incorporating HT two months prior to radiation, following standard clinical practice [69], (ii) administering EBRT alone, and (iii) applying HDR-BT alone. This comparative approach aimed to assess the impact of HT and RT modality on tumour shrinkage and PSA dynamics in each patient.

The analysis of Patient B (Table 6) shows that the combination of EBRT and HDR-BT achieved the highest tumour shrinkage (35.22%) and the lowest PSA (0.075 ng/mL), highlighting its strong efficacy in controlling tumour growth and PSA levels. HDR-BT alone showed a similar response, with a maximum shrinkage of 35.33% and a minimum PSA of 0.080 ng/mL, suggesting that HDR-BT is an important contributor to treatment success. In contrast, HT combined with EBRT and HDR-BT for three months resulted in a slightly lower shrinkage (32.31%) and a higher minimum PSA (0.338 ng/mL), indicating a slower response. Notably, the time to reach the lowest PSA was longest

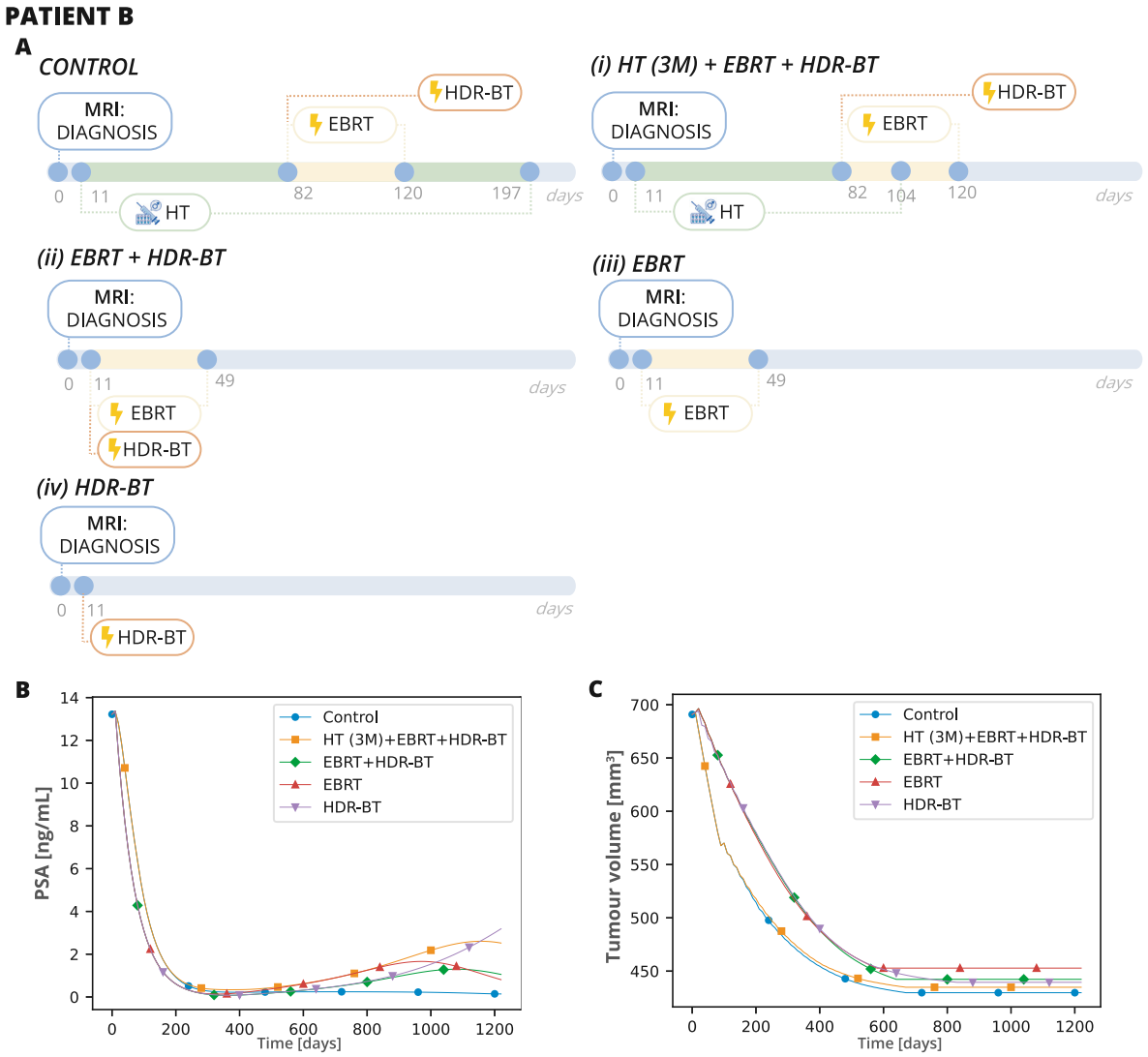

Fig. 5. Analysis of Patient B under different treatment strategies. (A) Overview of the treatment plans and their timelines. The control treatment represents the actual plan applied to this patient (six months of HT, followed by the concurrent administration of EBRT and HDR-BT). Alternative strategies include (i) reducing HT to three months before initiating EBRT and HDR-BT while HT is still being administered, (ii) omitting HT and proceeding directly with the concurrent administration of HDR-BT and EBRT, (iii) administering EBRT alone, and (iv) administering HDR-BT alone. (B) Predicted PSA dynamics for each treatment strategy. (C) Estimated tumour volume evolution under the different treatment strategies.

for the HT-based treatments (197 days), suggesting that while HT prolongs PSA suppression, it may not significantly improve tumour shrinkage. The PSA and tumour volume plots support these findings (Fig. 5 **B** and **C**). The curves for EBRT + HDR-BT and HDR-BT alone show a steep decline in PSA levels and tumour volume, stabilising at lower levels over time. Conversely, the HT-containing treatments show a more gradual decline, with PSA levels remaining slightly higher. The control treatment (HT for six months + EBRT + HDR-BT) achieved the lowest PSA of 0.141 ng/mL, which is lower than HT (3M) + EBRT + HDR-BT, but still higher than the non-HT regimens. This suggests that HT affects PSA kinetics but does not necessarily increase tumour shrinkage. The computational 3D tumour geometries illustrating the treatment outcomes for these therapeutic combinations are shown in Fig. S1 (top).

For Patient C, the treatment responses exhibited greater variability (Fig. 6 and Table 7). The control treatment (EBRT + HDR-BT) resulted in a reduction in tumour size of 34.70%, a PSA half-life of 44.94 days, and a very low minimum PSA (0.0007 ng/mL) at 680 days. The addition of HT for a period of six months prior to the beginning of RT resulted in a enhancement of the response, characterised by an increase in shrinkage to 36.48%, a prolongation of the PSA half-life to 66.29 days, and a slightly elevated minimum PSA (0.0028 ng/mL) at 650 days. However, the most concerning outcome was observed in the EBRT-only treatment, where shrinkage was drastically lower (19.10%), the PSA half-life was much longer (139 days), and the minimum PSA was exceptionally high (4.7643 ng/mL). Furthermore, this treatment failed to maintain control over disease progression, with PSA rising

Table 7
Analysis of patient C computational results for different treatment strategies. It includes the maximum percentage of tumour volume shrinkage, the time to PSA half-life, the time to decay below a threshold of 0.5 ng/mL and the minimum PSA.

Treatment	Max Shrinkage [%]	PSA Half-Life [days]	Time to Threshold [days]	PSA min [ng/mL]
Control	34.70	44.94	187.35	0.0007
HT(6M)+ EBRT+HDR-BT	36.48	66.29	211.08	0.0028
EBRT	19.10	138.63	–	4.7643
HDR-BT	33.75	44.94	187.36	0.0008

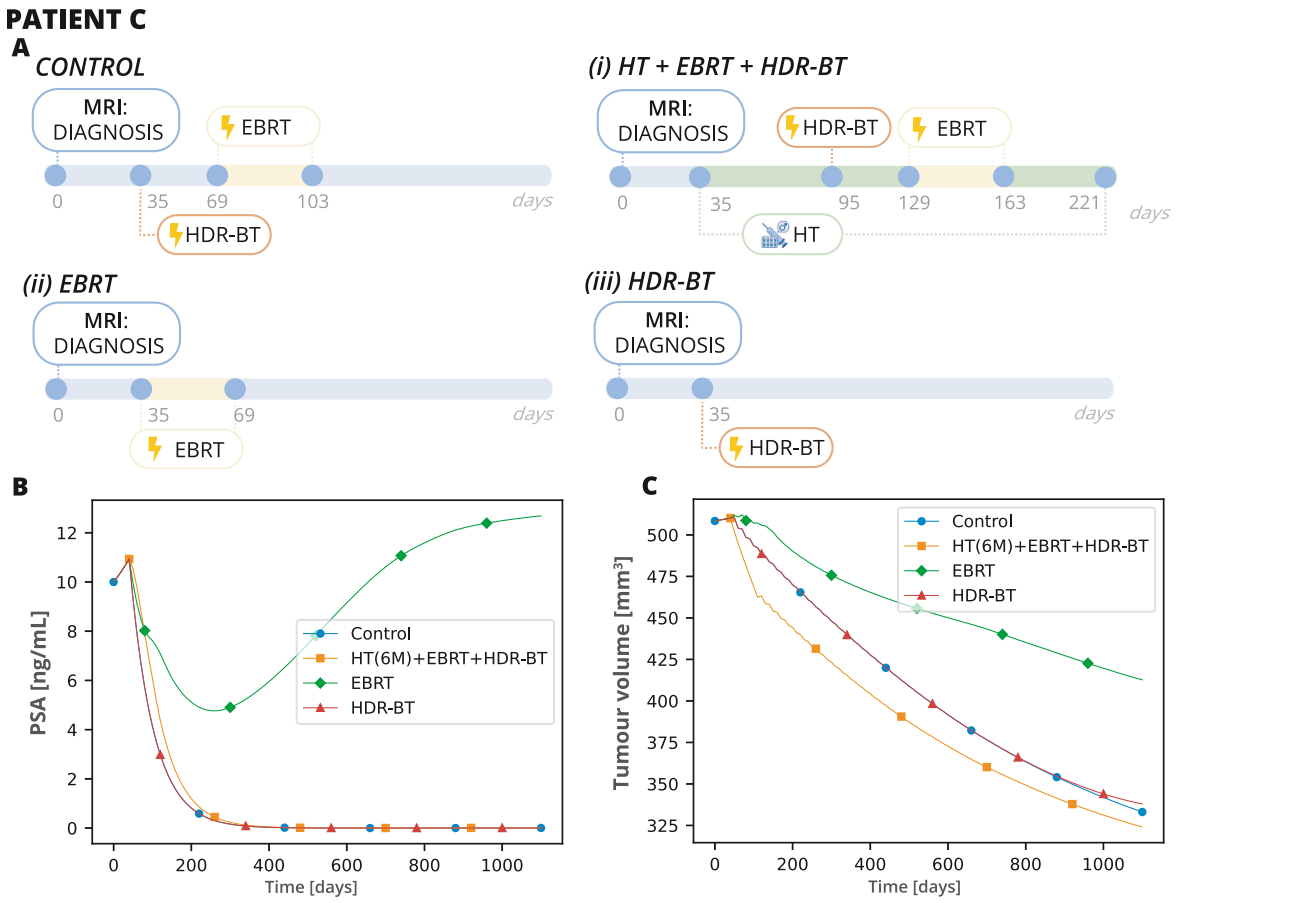

Fig. 6. Analysis of Patient C under different treatment strategies. (A) Overview of the treatment plans and their timelines. The control treatment corresponds to the actual plan applied to this patient, consisting of EBRT and HDR-BT. Alternative strategies include (i) incorporating HT for six months, (ii) administering EBRT alone, and (iii) applying HDR-BT alone. (B) Predicted PSA dynamics for each treatment strategy. (C) Estimated tumour volume evolution under the different treatment strategies.

rapidly to 12.6 ng/mL by the end of the simulation. Conversely, HDR-BT exhibited a comparable efficacy to the control group, achieving a reduction in tumour size of 33.75% and a minimum PSA concentration of 0.0008 ng/mL at 680 days, thereby validating its therapeutic potential in this patient population. The computational 3D tumour geometries illustrating the treatment outcomes for these therapeutic combinations are shown in Fig. S1 (bottom).

A comparative analysis of the two patients revealed that Patient B demonstrated greater tumour shrinkage across all treatment modalities, with EBRT alone exhibiting particular efficacy. In contrast, Patient C exhibited a more pronounced and sustained PSA suppression. The combination of EBRT and HDR-BT yielded favourable outcomes for both patients; however, Patient C demonstrated significantly lower PSA values, indicating a more profound biochemical response. The PSA half-life was faster in Patient B, suggesting a quicker response to treatment in terms of PSA kinetics. In contrast, Patient C exhibited a prolonged time to PSA half-life, which may indicate a more sustained response. The role of HT was more evident in Patient C, where it improved shrinkage and slowed PSA progression, while in Patient B, its effects were less pronounced. It can be hypothesised that these observations may reflect differences in the aggressiveness of the tumours. Patient C's more sustained PSA suppression, slower PSA half-life, and need for intensified treatment align with the characteristics of his PIRADS 5 score, which is indicative of a more aggressive tumour. In contrast, Patient B's PIRADS 4 score suggests a less aggressive tumour, consistent with his faster response and greater tumour shrinkage.

4. Discussion

This work extends the study presented in Pérez-Benito et al. [39], which introduced a patient-specific model for PCa tumour growth. The focus here is on the tumour's response to the most common treatments for PCa - HT, HDR-BT and EBRT-, with particular emphasis on PSA dynamics, as PSA is the primary biomarker used to evaluate tumour response to therapy. In contrast to the previous model, which was limited to patients under AS and did not incorporate therapeutic effects, the current study introduces several key advances. These include the simulation of treatment-specific spatial and temporal dynamics, the modelling of androgen transport as a new variable influencing tumour behaviour under hormone therapy, and the incorporation of a compartment for lethally damaged cells to better capture post-radiotherapy tumour response. These additions contribute to a more comprehensive and clinically relevant framework, allowing for the evaluation of combination therapies in patients undergoing active treatment.

The model considers three coexisting constituents, taking into account the nature of the prostate: healthy cells, stroma and, in areas defined as tumour, tumoural cells. The model assumes that cell proliferation and cell death are regulated by the concentration of specific tissue species (oxygen and androgens): sufficient concentration triggers proliferation, while its absence induces cell death. Since prostate cancer cells are heavily reliant on androgens for growth and survival, it is biologically plausible to model androgen concentration as a key driver in the evolution of tumoural cells [14,16,41]. In this way, HT lowers the level of androgens in the blood, so that the androgens that reach the tissues are not sufficient for the tumoural cells to survive. The time

these levels takes to return to normal after treatment is stopped is also taken into account [42]. Conversely, healthy cells and stroma exhibit lower sensitivity to androgen levels [70,71].

To model the cellular response to radiation, the LQ model is employed, a widely recognised and established framework for simulating RT effects. This model predicts cellular responses to ionising radiation, providing a straightforward relationship between cell survival and the radiation dose delivered [43]. It is particularly effective for modelling the effects of EBRT, where the total dose is divided into smaller fractions to minimise damage to surrounding healthy tissues. This fractionation allows healthy cells adequate time to recover between doses, ensuring that sub-lethal damage from the initial exposure is fully repaired, and the cells behave as if they had not been irradiated at all. However, the LQ model has limitations at high doses, where its predictions for cell death become less accurate [44–46,72,73]. To address this, a modification to the standard LQ model, known as the LQ-L model, is applied. This adjustment better aligns with the observed biological response of cells at higher doses, where the assumption of proportional damage no longer holds [47].

Furthermore, since cells do not immediately die upon exposure to RT [48], a new constituent is introduced: lethally damaged cells. These are cells that, despite receiving radiation, cannot repair the damage and ultimately die after a characteristic time period [62]. Although these cells contribute to the overall tumour volume, it is assumed in the model that they are incapable of producing PSA, a key biomarker for tumour activity. In this model, it is hypothesised that healthy cells completely recover after radiation exposure, and only tumoural cells are considered to be affected by the treatment [74]. This assumption simplifies the model by focusing on the tumour's response to RT, which is the primary concern for treatment planning and effectiveness. The model also accounts for damage to cell proliferation capacity caused by RT, taking into account the typical recovery time from the last moment of treatment.

The computation of PSA in the tissue involves considering that in the tumour area, where lumens and ducts are obstructed due to abnormal cell proliferation, the accumulation of PSA in the tissue surpasses that in the healthy region [40,75]. To account for this effect and as a simplification, it is assumed that only tumoural cells produce PSA.

Seven patients from routine clinical practice are used to test this novel methodology. As the patients were selected from a retrospective study, the available data are limited. In the clinical practice, PSA blood tests are typically performed every three to six months after treatment to monitor tumour progression. While this frequency is sufficient for clinical purposes, it is lacking for detailed analysis using *in-silico* models such as the one proposed here. In addition, there are often no data available between the first MRI scan and the start of treatment. In standard practice, the PSA level is the primary diagnostic indicator. If an elevated PSA suggests the possibility of cancer, an MRI and biopsy are performed, and if cancer is confirmed, treatment is started immediately. If treatment appears to be successful and there is no sign of recurrence, follow-up MRIs after treatment are rarely performed. Therefore, due to the nature of the patients included in this retrospective study—who were classified as intermediate-risk and demonstrated favourable responses to therapy—follow-up MRIs were not conducted. As a result, post-treatment tumour geometry was not available, preventing direct validation of tumour evolution using imaging data.

In view of these limitations, the focus of the study is on modelling the effect of treatments on the basis of their influence on PSA dynamics. Patient A was chosen to calibrate the specific parameters of the model related to PSA production by tumoural cells and PSA decay in tissue, values for which reliable data are scarce in the literature. This patient was selected because sufficient pre- and post-treatment PSA measurements were available for calibration. Although no PSA data were recorded between the initial MRI diagnosis and the start of treatment, the available PSA values were fitted to an exponential curve to generate synthetic data points for optimisation purposes. Once the general parameters of the model had been defined using patient A, it is run on six additional patients. The results show that the model successfully reproduces PSA dynamics. Specifically, the observed decline in PSA levels was associated with tumour cell death. As the concentration of tumoural cells decreases, PSA production becomes negligible, leading to a situation where PSA is cleared from the tissue faster than it is produced. The decline in PSA levels is a well-documented consequence of treatment [76–78]. Consequently, the model provides an estimate of tumour shrinkage based on the observed PSA dynamics, providing a valuable tool for understanding the relationship between tumour cell behaviour and PSA response to treatment.

In parallel, a sensitivity analysis is conducted to assess the impact of key model parameters on tumour progression and PSA response. Although not included in the main text due to focus and space considerations, the Supplementary Material provides the results of a global sensitivity analysis based on the Morris screening method. For the local sensitivity analysis based on parameter optimisation, we refer the reader to our previous work [39], where this approach is applied and discussed in detail.

The model attains patient-specificity by integrating individualised clinical data from MRIs and biopsies, which directly influence the predictions, despite employing a unified parameter set calibrated on a single patient. This approach captures inter-patient variability through personalised inputs rather than per-patient parameter tuning [19]. Given the heterogeneity of treatment strategies in our cohort—where nearly every patient received a unique combination of therapies—stratifying the calibration by treatment type would not be feasible and would ultimately result in a distinct parameter set for each patient. Moreover, since the immediate post-treatment PSA response typically follows a consistent pattern across modalities—characterised by a sharp decline—the benefits of separate calibrations per treatment type are limited in this context. By relying on general parameters and patient-specific input data, our approach avoids overfitting, enhances reproducibility, and streamlines clinical integration while still enabling personalised predictions. This work represents a first approximation; future studies should explore cross-calibration strategies and model stratification by treatment type to further assess the robustness and generalisability of the model.

It is important to note that the imaging data used in this study were obtained retrospectively from routine clinical practice, where the primary objective was patient evaluation rather than research standardisation. As such, variations in acquisition protocols reflect the realities of clinical imaging workflows. Nevertheless, the importance of protocol harmonisation for future research applications is recognised and emphasise the need for more standardised imaging acquisition in prospective studies to enhance consistency and reproducibility.

The predictive capability of the model was evaluated using the MAE and the RMSE. These metrics provide complementary insights into the accuracy of the simulated PSA dynamics relative to clinical data, with RMSE offering greater sensitivity to larger deviations. While percentage-based error metrics, such as the Mean Absolute Percentage Error (MAPE), could offer a standardised approach to compare model performance across patients, their application is limited in this context. This is primarily due to the fact that post-treatment PSA values are frequently close to zero, which may lead to numerically unstable or inflated percentage errors. As such, absolute error metrics were deemed more appropriate for assessing model accuracy in the present study.

In order to more accurately estimate the model's capacity to assess tumour response to various treatments, a comparative analysis of treatment strategies is conducted in two distinct patients. The results of this analysis highlight the significant impact of patient-specific factors on treatment efficacy, underscoring the limitations of a universally applicable approach. For Patient B, the employment of diverse radiation strategies led to comparable outcomes, suggesting a greater degree of

treatment flexibility. Conversely, Patient C exhibited an unfavourable response to EBRT alone, characterised by rapid PSA progression, underscoring the importance of combination or alternative therapies for effective disease management. HDR-BT proved to be a highly effective treatment in both patients, either as a standalone modality or in combination with other treatments, while prolonged HT did not consistently demonstrate added benefit. In conclusion, these findings underscore the need for personalised treatment strategies that are tailored to individual patient responses to ensure optimal outcomes in the treatment of PCa [79,80]. The observed variations in response may be associated with the patient's PIRADS classification. Patient B, who was classified as PIRADS 4, exhibited enhanced tumour shrinkage and accelerated PSA decline, indicating a less aggressive tumour [81,82]. In contrast, Patient C, who was classified as PIRADS 5, demonstrated a more pronounced biochemical response but demonstrated PSA progression with EBRT alone. This suggests that Patient C harbours a more aggressive tumour, potentially resistant to radiation, and is more likely to benefit from combination therapies [83].

In order to gain a deeper understanding of the mechanisms involved in tumour development, access to additional data is essential, though currently unavailable. Acquiring comprehensive datasets for such analyses is challenging, as retrospective studies often rely on data from patients treated in hospitals, where non-invasive tests are prioritised to ensure patient safety and comfort. Improving treatment outcomes and quality of life remains a key objective, and projects such as CHAIMELEON [84], ProCAncer-I [85] and ProCanAid [86] aim to address data limitations. CHAIMELEON [84] focuses on establishing a cancer imaging repository containing large, high-quality anonymised datasets, including prostate cancer cases. In contrast, ProCAncer-I [85] is developing an extensive, interoperable medical image repository and advancing artificial intelligence models to support diagnosis, metastasis detection, and treatment response prediction. These datasets are crucial for the future development and refinement of computational models, enabling more accurate simulations of tumour growth and treatment response. ProCanAid [86], in addition to the patient database, goes a step further with the aim of developing a computational tool to create a 4D digital twin of the entire prostate of a patient.

In summary, this study highlights the valuable role of computational modelling in enhancing our understanding of PCa growth and treatment response, particularly in relation to PSA dynamics. Such models serve as powerful tools to support clinical decision-making by enabling personalised treatment planning and prediction of therapeutic outcomes. This work represents an initial contribution to the development of a future digital PCa twin. In the future, patient-specific digital twins for PCa could provide clinicians with robust tools to predict disease progression on an individual basis, facilitating the selection of the most appropriate treatment strategies and minimising the risk of both over- and under-treatment, which can cause significant patient distress. Future extensions of the model could incorporate additional biological mechanisms such as the immune response, further improving predictive accuracy. Ultimately, integrating digital twins into clinical workflows holds great promise for advancing precision medicine, improving treatment outcomes, and enhancing patients' quality of life.

CRediT authorship contribution statement

Ángela Pérez-Benito: Writing – review & editing, Writing – original draft, Visualization, Validation, Software, Methodology, Investigation, Data curation. **Adrián Galiana-Bordera:** Writing – review & editing, Resources, Data curation. **Pedro-Miguel Martínez-Gironés:** Writing – original draft, Resources, Data curation. **Gemma Urbanos:** Writing – review & editing, Data curation. **Anna Nogué Infante:** Writing – review & editing, Data curation. **María José Gómez-Benito:** Writing – review & editing, Supervision, Resources, Methodology, Investigation, Funding acquisition. **María Ángeles Pérez:** Writing – review & editing, Supervision, Resources, Project administration, Methodology, Investigation, Funding acquisition, Conceptualization.

Ethics statement

No animal studies are presented in this manuscript. The studies involving humans were approved by Técnica del Comité de Ética de la Investigación con medicamentos del CEIM - HOSPITAL UNIVERSITARIO Y POLITÉCNICO LA FE. The studies were conducted in accordance with the local legislation and institutional requirements. Written informed consent for participation was not required from the participants or the participants' legal guardians/next of kin in accordance with the national legislation and institutional requirements. No potentially identifiable images or data are presented in this study.

Declaration of Generative AI and AI-assisted technologies in the writing process

During the preparation of this work the author(s) used ChatGPT 4o in order to improve language and readability. After using this tool/service, the author(s) reviewed and edited the content as needed and take(s) full responsibility for the content of the publication.

Declaration of competing interest

The authors declare that they have no known competing financial interests or personal relationships that could have appeared to influence the work reported in this paper.

Acknowledgements

We would like to express our gratitude to the rest of collaborators from La Fe Hospital (HULAFE) & Biomedical Imaging Research Group (GIBI230), Quibim S.L. for their essential contribution in retrieving, annotating and processing the patient specific imaging and clinical data required for the development of this work, and Multiscale in Mechanical and Biological Engineering (M2BE) group from the University of Zaragoza. This study was funded by ProCanAid (Digital twin for aided detection, diagnosis of prostate cancer and simulation of the effects and effectiveness of different oncological treatments), a R&D Strategic Areas MICINN 2021 project (Spanish Science Agency - Ministry of Science), Grant No. PLEC2021-007709. The authors also acknowledge the support of the Aragon Government through Group T50 23R.

Appendix A. Supplementary data

Supplementary material related to this article can be found online at https://doi.org/10.1016/j.cmpb.2025.108931.

References

[1] International Agency for Research on Cancer (IARC), Cancer tomorrow dataviz, 2024.

[2] G. Lorenzo, M.A. Scott, K. Tew, T.J.R. Hughes, Y.J. Zhang, L. Liu, G. Vilanova, H. Gómez, Tissue-scale, personalized modeling and simulation of prostate cancer growth, Proc. Natl. Acad. Sci. 113 (48) (2016) E7663–E7671, http://dx.doi.org/10.1073/pnas.1615791113.

[3] R.J. Rebello, C. Oing, K.E. Knudsen, S. Loeb, D.C. Johnson, R.E. Reiter, S. Gillessen, T.V. der Kwast, R.G. Bristow, Prostate cancer, Nat. Rev. Dis. Prim. 7 (2021) http://dx.doi.org/10.1038/s41572-020-00243-0.

[4] B. Turkbey, A.B. Rosenkrantz, M.A. Haider, A.R. Padhani, G. Villeirs, K.J. Macura, C.M. Tempany, P.L. Choyke, F. Cornud, D.J. Margolis, et al., Prostate imaging reporting and data system version 2.1: 2019 update of prostate imaging reporting and data system version 2, Eur. Urol. 76 (3) (2019) 340–351, http://dx.doi.org/10.1016/j.eururo.2019.02.033.

[5] J.C. Weinreb, J.O. Barentsz, P.L. Choyke, F. Cornud, M.A. Haider, K.J. Macura, D. Margolis, M.D. Schnall, F. Shtern, C.M. Tempany, H.C. Thoeny, S. Verma, PI-RADS prostate imaging - reporting and data system: 2015, version 2, Eur. Urol. 69 (2016) 16–40, http://dx.doi.org/10.1016/j.eururo.2015.08.052.

[6] J.I. Epstein, M.J. Zelefsky, D.D. Sjoberg, J.B. Nelson, L. Egevad, C. Magi-Galluzzi, A.J. Vickers, A.V. Parwani, V.E. Reuter, S.W. Fine, J.A. Eastham, P. Wiklund, M. Han, C.A. Reddy, J.P. Ciezki, T. Nyberg, E.A. Klein, A contemporary prostate cancer grading system: A validated alternative to the gleason score, Eur. Urol. 69 (2016) 428–435, http://dx.doi.org/10.1016/j.eururo.2015.06.046.

[7] European Association of Urology (EAU), Prostate cancer: Classification and staging systems, 2024, (Accessed 17 December 2024), https://uroweb.org/guidelines/prostate-cancer/chapter/classification-and-staging-systems#note_94.

[8] I. Gómez-Acebo, T. Dierssen-Sotos, P. Fernandez-Navarro, C. Palazuelos, V. Moreno, N. Aragonés, G. Castaño-Vinyals, J.J. Jiménez-Monleón, J.L. Ruiz-Cerdá, B. Pérez-Gómez, J.M. Ruiz-Dominguez, J.A. Molero, M. Pollán, M. Kogevinas, J. Llorca, Risk model for prostate cancer using environmental and genetic factors in the spanish multi-case-control (MCC) study, Sci. Rep. 7 (1) (2017) 8994, http://dx.doi.org/10.1038/s41598-017-09386-9.

[9] M.S. Litwin, H.J. Tan, The diagnosis and treatment of prostate cancer: A review, JAMA 317 (2017) 2532–2542, http://dx.doi.org/10.1001/jama.2017.7248.

[10] S. Asif, B.A. Teply, Biomarkers for treatment response in advanced prostate cancer, Cancers 13 (22) (2021) http://dx.doi.org/10.3390/cancers13225723.

[11] J.-Y. Chen, P.-Y. Wang, M.-Z. Liu, F. Lyu, M.-W. Ma, X.-Y. Ren, X.-S. Gao, Biomarkers for prostate cancer: From diagnosis to treatment, Diagnostics 13 (21) (2023) http://dx.doi.org/10.3390/diagnostics13213350.

[12] J. Xiao, M. Zhang, D. Wu, Side effects of prostate cancer therapies and potential management, J. Biological Methods 11 (3) (2024) e99010018, http://dx.doi.org/10.14440/jbm.2024.0019.

[13] M. Hadjicharalambous, Y. Roussakis, G. Bourantas, E. Ioannou, K. Miller, P. Doolan, I. Strouthos, C. Zamboglou, V. Vavourakis, Personalised in silico biomechanical modelling towards the optimisation of high dose-rate brachytherapy planning and treatment against prostate cancer, Front. Physiol. 15 (2024) http://dx.doi.org/10.3389/fphys.2024.1491144.

[14] C. Huggins, C.V. Hodges, Studies on prostatic cancer: I. The effect of castration, of estrogen and of androgen injection on serum phosphatases in metastatic carcinoma of the prostate, Cancer Res. 1 (4) (1941) 293–297, http://dx.doi.org/10.1016/S0022-5347(05)64820-3.

[15] J.M. Martínez-Jabaloyas, J.L. Ruiz-Cerdá, M. Hernández, A. Jiménez, F. Jiménez-Cruz, Prognostic value of DNA ploidy and nuclear morphometry in prostate cancer treated with androgen deprivation, Urology 59 (5) (2002) 715–720, http://dx.doi.org/10.1016/S0090-4295(02)01530-3.

[16] C. Dai, S.M. Dehm, N. Sharifi, Targeting the androgen signaling axis in prostate cancer, J. Clin. Oncol. 41 (26) (2023) 4267–4278, http://dx.doi.org/10.1200/JCO.23.00433.

[17] A.J. Conde-Moreno, F. López-Campos, A. Hervás, V. Morillo, A. Méndez, M.D.M. Puertas, J. Valero-Albarrán, A. Gómez Iturriaga, M. Rico, M.L. Vázquez, P.M. Samper Ots, L.A. Perez-Romasanta, J. Pastor, C. Ibáñez, F. Ferrer, A. Zapatero, A.S. García-Blanco, A. Rodríguez, C. Ferrer, A phase II trial of stereotactic body radiation therapy and androgen deprivation for oligometastases in prostate cancer (SBRT-SG 05), Pr. Radiat. Oncol. 14 (5) (2024) e344–e352, http://dx.doi.org/10.1016/j.prro.2024.04.022.

[18] A. Karolak, D.A. Markov, L.J. McCawley, K.A. Rejniak, Towards personalized computational oncology: from spatial models of tumour spheroids, to organoids, to tissues, J. R. Soc. Interface 15 (138) (2018) 20170703, http://dx.doi.org/10.1098/rsif.2017.0703.

[19] S. Hervás-Raluy, D. Sainz-DeMena, M.J. Gómez-Benito, J.M. García-Aznar, Image-based biomarkers for engineering neuroblastoma patient-specific computational models, Eng. Comput. (2024) http://dx.doi.org/10.1007/s00366-024-01964-6.

[20] N.C. Atuegwu, L.R. Arlinghaus, X. Li, A.B. Chakravarthy, V.G. Abramson, M.E. Sanders, T.E. Yankeelov, Parameterizing the logistic model of tumor growth by DW-MRI and DCE-MRI data to predict treatment response and changes in breast cancer cellularity during neoadjuvant chemotherapy, Transl. Oncol. 6 (2013) 256–264, http://dx.doi.org/10.1593/tlo.13130.

[21] L. Schmiester, F. Brasó-Maristany, B. González-Farré, T. Pascual, J. Gavilá, X. Tekpli, J. Geisler, V.N. Kristensen, A. Frigessi, A. Prat, et al., Computational model predicts patient outcomes in luminal b breast cancer treated with endocrine therapy and CDK4/6 inhibition, Clin. Cancer Res. 30 (17) (2024) 3779–3787, http://dx.doi.org/10.1158/1078-0432.CCR-24-0244.

[22] M. Hadjicharalambous, P.A. Wijeratne, V. Vavourakis, From tumour perfusion to drug delivery and clinical translation of in silico cancer models, Methods 185 (2021) 82–93, http://dx.doi.org/10.1016/j.ymeth.2020.02.010.

[23] R.A. Bekker, S. Kim, S. Pilon-Thomas, H. Enderling, Mathematical modeling of radiotherapy and its impact on tumor interactions with the immune system, Neoplasia 28 (2022) 100796, http://dx.doi.org/10.1016/j.neo.2022.100796.

[24] C. Sosa-Marrero, R.D. Crevoisier, A. Hernandez, P. Fontaine, N. Rioux-Leclercq, R. Mathieu, A. Fautrel, F. Paris, O. Acosta, Towards a reduced in silico model predicting biochemical recurrence after radiotherapy in prostate cancer, IEEE Trans. Biomed. Eng. 68 (2021) 2718–2729, http://dx.doi.org/10.1109/TBME.2021.3052345.

[25] M.F. Farayola, S. Shafie, F.M. Siam, I. Khan, Mathematical modeling of radiotherapy cancer treatment using Caputo fractional derivative, Comput. Methods Programs Biomed. 188 (2020) http://dx.doi.org/10.1016/j.cmpb.2019.105306.

[26] S. Apeke, L. Gaubert, N. Boussion, P. Lambin, D. Visvikis, V. Rodin, P. Redou, Multi-scale modeling and oxygen impact on tumor temporal evolution: Application on rectal cancer during radiotherapy, IEEE Trans. Med. Imaging 37 (4) (2017) 871–880, http://dx.doi.org/10.1109/TMI.2017.2771379.

[27] G. Lorenzo, T.J. Hughes, A. Reali, H. Gómez, A numerical simulation study of the dual role of 5α-reductase inhibitors on tumor growth in prostates enlarged by benign prostatic hyperplasia via stress relaxation and apoptosis upregulation, Comput. Methods Appl. Mech. Engrg. 362 (2020) http://dx.doi.org/10.1016/j.cma.2020.112843.

[28] R. Brady-Nicholls, J.D. Nagy, T.A. Gerke, T. Zhang, A.Z. Wang, J. Zhang, R.A. Gatenby, H. Enderling, Prostate-specific antigen dynamics predict individual responses to intermittent androgen deprivation, Nat. Commun. 11 (1) (2020) 1750, http://dx.doi.org/10.1038/s41467-020-15424-4.

[29] H.V. Jain, S.K. Clinton, A. Bhinder, A. Friedman, Mathematical modeling of prostate cancer progression in response to androgen ablation therapy, Proc. Natl. Acad. Sci. 108 (49) (2011) 19701–19706, http://dx.doi.org/10.1073/pnas.1115750108.

[30] A.M. Ideta, G. Tanaka, T. Takeuchi, K. Aihara, A mathematical model of intermittent androgen suppression for prostate cancer, J. Nonlinear Sci. 18 (2008) 593–614, http://dx.doi.org/10.1007/s00332-008-9031-0.

[31] G. Lorenzo, V.M. Pérez-García, A. Mariño, L.A. Pérez-Romasanta, A. Reali, H. Gómez, Mechanistic modelling of prostate-specific antigen dynamics shows potential for personalized prediction of radiation therapy outcome, J. R. Soc. Interface 16 (2019) http://dx.doi.org/10.1098/RSIF.2019.0195.

[32] L. Martí-Bonmatí, A. Alberich-Bayarri, Imaging Biomarkers: Development and Clinical Integration, Springer, 2016.

[33] D. Sainz-DeMena, W. Ye, M.Á. Pérez, J.M. García-Aznar, A finite element based optimization algorithm to include diffusion into the analysis of DCE-mri, Eng. Comput. 38 (5) (2022) 3849–3865, http://dx.doi.org/10.1007/s00366-022-01667-w.

[34] D. Sainz-DeMena, M. Pérez, J. García-Aznar, Exploring the potential of physics-informed neural networks to extract vascularization data from DCE-mri in the presence of diffusion, Med. Eng. Phys. 123 (2024) 104092, http://dx.doi.org/10.1016/j.medengphy.2023.104092.

[35] R. Sanz-Requena, L. Martí-Bonmatí, R. Pérez-Martínez, G. García-Martí, Dynamic contrast-enhanced case-control analysis in 3T MRI of prostate cancer can help to characterize tumor aggressiveness, Eur. J. Radiol. 85 (11) (2016) 2119–2126, http://dx.doi.org/10.1016/j.ejrad.2016.09.022.

[36] N. Kronik, Y. Kogan, M. Elishmereni, K. Halevi-Tobias, S. Vuk-Pavlović, Z. Agur, Predicting outcomes of prostate cancer immunotherapy by personalized mathematical models, PloS One 5 (12) (2010) e15482, http://dx.doi.org/10.1371/journal.pone.0015482.

[37] G. Lorenzo, N. di Muzio, C.L. Deantoni, C. Cozzarini, A. Fodor, A. Briganti, F. Montorsi, V.M. Pérez-García, H. Gomez, A. Reali, Patient-specific forecasting of postradiotherapy prostate-specific antigen kinetics enables early prediction of biochemical relapse, IScience 25 (11) (2022) 105430, http://dx.doi.org/10.1016/j.isci.2022.105430.

[38] G. Lorenzo, J.S. Heiselman, M.A. Liss, M.I. Miga, H. Gomez, T.E. Yankeelov, A. Reali, T.J. Hughes, A pilot study on patient-specific computational forecasting of prostate cancer growth during active surveillance using an imaging-informed biomechanistic model, Cancer Res. Commun. 4 (3) (2024) 617–633, http://dx.doi.org/10.1158/2767-9764.CRC-23-0449.

[39] Á. Pérez-Benito, J.M. García-Aznar, M.J. Gómez-Benito, M.Á. Pérez, Patient-specific prostate tumour growth simulation: a first step towards the digital twin, Front. Physiol. 15 (2024) 1421591, http://dx.doi.org/10.3389/fphys.2024.1421591.

[40] H. Lilja, D. Ulmert, A.J. Vickers, Prostate-specific antigen and prostate cancer: Prediction, detection and monitoring, Nat. Rev. Cancer 8 (2008) 268–278, http://dx.doi.org/10.1038/nrc2351.

[41] T.-H. Li, H. Zhao, Y. Peng, J. Beliakoff, J.D. Brooks, Z. Sun, A promoting role of androgen receptor in androgen-sensitive and -insensitive prostate cancer cells, Nucleic Acids Res. 35 (8) (2007) 2767–2776, http://dx.doi.org/10.1093/nar/gkm198.

[42] J. Planas, A. Celma, J. Placer, M. Cuadras, L. Regis, C. Gasanz, E. Trilla, C. Salvador, D. Lorente, J. Morote, Hormonal response recovery after long-term androgen deprivation therapy in patients with prostate cancer, Scand. J. Urol. 50 (6) (2016) 425–428, http://dx.doi.org/10.1080/21681805.2016.1227876.

[43] S.J. McMahon, The linear quadratic model: Usage, interpretation and challenges, Phys. Med. Biol. 64 (2019) http://dx.doi.org/10.1088/1361-6560/aaf26a.

[44] C. Park, L. Papiez, S. Zhang, M. Story, R.D. Timmerman, Universal survival curve and single fraction equivalent dose: Useful tools in understanding potency of ablative radiotherapy, Int. J. Radiat. Oncol. Biol. Phys. 70 (2008) 847–852, http://dx.doi.org/10.1016/j.ijrobp.2007.10.059.

[45] J.Z. Wang, X.A. Li, C.X. Yu, S.J. DiBiase, The low α/β ratio for prostate cancer: What does the clinical outcome of HDR brachytherapy tell us? Int. J. Radiat. Oncol. Biol. Phys. 57 (2003) 1101–1108, http://dx.doi.org/10.1016/S0360-3016(03)00747-8.

[46] M. Cui, X.S. Gao, X. Li, M. Ma, X. Qi, Y. Shibamoto, Variability of α/β ratios for prostate cancer with the fractionation schedule: caution against using the linear-quadratic model for hypofractionated radiotherapy, Radiat. Oncol. 17 (2022) http://dx.doi.org/10.1186/s13014-022-02010-9.

[47] M. Astrahan, Some implications of linear-quadratic-linear radiation dose-response with regard to hypofractionation, Med. Phys. 35 (2008) 4161–4172, http://dx.doi.org/10.1118/1.2969065.
[48] A. Van Der Kogel, M. Joiner, Basic Clinical Radiobiology, Oxford University Press, 2009.
[49] A. Carlos-Reyes, M.A. Muñiz-Lino, S. Romero-Garcia, C. López-Camarillo, O.N. Hernández-de la Cruz, Biological adaptations of tumor cells to radiation therapy, Front. Oncol. 11 (2021) http://dx.doi.org/10.3389/fonc.2021.718636.
[50] J.J. Kim, I.F. Tannock, Repopulation of cancer cells during therapy: An important cause of treatment failure, Nat. Rev. Cancer 5 (2005) 516–525, http://dx.doi.org/10.1038/nrc1650.
[51] A. Nieto, J. Escribano, F. Spill, J.M. García-Aznar, M.J. Gómez-Benito, Finite element simulation of the structural integrity of endothelial cell monolayers: A step for tumor cell extravasation, Eng. Fract. Mech. 224 (2020) 106718, http://dx.doi.org/10.1016/j.engfracmech.2019.106718.
[52] A. Agosti, C. Cattaneo, C. Giverso, D. Ambrosi, P. Ciarletta, A computational framework for the personalized clinical treatment of glioblastoma multiforme, J. Appl. Math. Mech. (2018) http://dx.doi.org/10.1002/zamm.201700294.
[53] S.R. McKeown, Defining normoxia, physoxia and hypoxia in tumours - implications for treatment response, Br. J. Radiol. 87 (2014) http://dx.doi.org/10.1259/bjr.20130676.
[54] C. Sosa-Marrero, R.D. Crevoisier, A. Hernandez, P. Fontaine, N. Rioux-Leclercq, R. Mathieu, A. Fautrel, F. Paris, O. Acosta, Towards a reduced in silico model predicting biochemical recurrence after radiotherapy in prostate cancer, IEEE Trans. Biomed. Eng. 68 (2021) 2718–2729, http://dx.doi.org/10.1109/TBME.2021.3052345.
[55] F. Mpekris, S. Angeli, A.P. Pirentis, T. Stylianopoulos, Stress-mediated progression of solid tumors: effect of mechanical stress on tissue oxygenation, cancer cell proliferation, and drug delivery, Biomech. Model. Mechanobiol. 14 (2015) 1391–1402, http://dx.doi.org/10.1007/s10237-015-0682-0.
[56] E.C. Faria, N. Ma, E. Gazi, P. Gardner, M. Brown, N.W. Clarke, R.D. Snook, Measurement of elastic properties of prostate cancer cells using AFM, Analyst 133 (2008) 1498–1500, http://dx.doi.org/10.1039/b803355b.
[57] M. Lekka, D. Gil, K. Pogoda, J. Dulińska-Litewka, R. Jach, J. Gostek, O. Klymenko, S. Prauzner-Bechcicki, Z. Stachura, J. Wiltowska-Zuber, K. Okoń, P. Laidler, Cancer cell detection in tissue sections using AFM, Arch. Biochem. Biophys. 518 (2012) 151–156, http://dx.doi.org/10.1016/j.abb.2011.12.013.
[58] A. Bharatha, M. Hirose, N. Hata, S.K. Warfield, M. Ferrant, K.H. Zou, E. Suarez-Santana, J. Ruiz-Alzola, A. D'Amico, R.A. Cormack, R. Kikinis, F.A. Jolesz, C.M. Tempany, Evaluation of three-dimensional finite element-based deformable registration of pre- and intraoperative prostate imaging, Med. Phys. 28 (2001) 2551–2560, http://dx.doi.org/10.1118/1.1414009.
[59] G. Lorenzo, T.J. Hughes, P. Domínguez-Frojan, A. Reali, H. Gómez, Computer simulations suggest that prostate enlargement due to benign prostatic hyperplasia mechanically impedes prostate cancer growth, Proc. Natl. Acad. Sci. USA 116 (2019) 1152–1161, http://dx.doi.org/10.1073/pnas.1815735116.
[60] F.H. Dall, C. s. Jørgensen, D. Houe, H. Gregersen, J.C. Djurhuus, Biomechanical wall properties of the human rectum. a study with impedance planimetry, Gut 34 (1993) 1581–1586, http://dx.doi.org/10.1136/gut.34.11.1581.
[61] X. Chai, M.V. Herk, J.B.V.D. Kamer, M.C. Hulshof, P. Remeijer, H.T. Lotz, A. Bel, Finite element based bladder modeling for image-guided radiotherapy of bladder cancer, Med. Phys. 38 (2011) 142–150, http://dx.doi.org/10.1118/1.3523624.
[62] V.M. Pérez-García, M. Bogdanska, A. Martínez-González, J. Belmonte-Beitia, P. Schucht, L.A. Pérez-Romasanta, Delay effects in the response of low-grade gliomas to radiotherapy: a mathematical model and its therapeutical implications, Math. Med. Biology: A J. the IMA 32 (3) (2015) 307–329, http://dx.doi.org/10.1093/imammb/dqu009.
[63] T. Akiba, S. Sano, T. Yanase, T. Ohta, M. Koyama, Optuna: A next-generation hyperparameter optimization framework, in: Proceedings of the 25th ACM SIGKDD International Conference on Knowledge Discovery and Data Mining, Association for Computing Machinery, 2019, pp. 2623–2631, http://dx.doi.org/10.1145/3292500.3330701,
[64] R.J. Karnes, F.R. MacKintosh, C.H. Morrell, L. Rawson, P.C. Sprenkle, M.W. Kattan, M. Colicchia, T.B. Neville, Prostate-specific antigen trends predict the probability of prostate cancer in a very large U.S. veterans affairs cohort, Front. Oncol. 8 (2018) http://dx.doi.org/10.3389/fonc.2018.00296.
[65] H. Siebinga, B.J.d. van der Veen, D.M. de Vries-Huizing, W.V. Vogel, J.J. Hendrikx, A.D. Huitema, Quantification of biochemical PSA dynamics after radioligand therapy with [177Lu]Lu-PSMA-I&T using a population pharmacokinetic/pharmacodynamic model, EJNMMI Phys. 11 (2024) http://dx.doi.org/10.1186/s40658-024-00642-2.
[66] A. Jímenez-Pastor, R. López-González, B. Fos-Guarinos, F. García-Castro, M. Wittenberg, A. Torregrosa-Andrés, L. Martí-Bonmatí, M. García-Fontes, P. Duarte, J.P. Gambini, L.K. Bittencourt, F.C. Kitamura, V.K. Venugopal, V. Mahajan, P. Ros, E. Soria-Olivas, A. Alberich-Bayarri, Automated prostate multi-regional segmentation in magnetic resonance using fully convolutional neural networks, Eur. Radiol. 33 (2023) 5087–5096, http://dx.doi.org/10.1007/s00330-023-09410-9.
[67] P.S. Tofts, A.G. Kermode, Measurement of the blood-brain barrier permeability and leakage space using dynamic MR imaging. 1. Fundamental concepts, Magn. Reson. Med. 17 (2) (1991) 357–367, http://dx.doi.org/10.1002/mrm.1910170208.
[68] D. Sainz-DeMena, J.M. García-Aznar, M.A. Pérez, C. Borau, Im2mesh: A python library to reconstruct 3D meshes from scattered data and 2D segmentations, application to patient-specific neuroblastoma tumour image sequences, Appl. Sci. 12 (22) (2022) http://dx.doi.org/10.3390/app122211557.
[69] D.-D. Nguyen, L. Haeuser, M. Paciotti, C. Reitblat, J. Cellini, S.R. Lipsitz, A.S. Kibel, A.D. Choudhury, E.B. Cone, Q.-D. Trinh, Systematic review of time to definitive treatment for intermediate risk and high risk prostate cancer: Are delays associated with worse outcomes? J. Urol. 205 (5) (2021) 1263–1274, http://dx.doi.org/10.1097/JU.0000000000001601.
[70] M. Singh, R. Jha, J. Melamed, E. Shapiro, S.W. Hayward, P. Lee, Stromal androgen receptor in prostate development and cancer, Am. J. Pathol. 184 (10) (2014) 2598–2607, http://dx.doi.org/10.1016/j.ajpath.2014.06.022.
[71] D.A. Leach, G. Buchanan, Stromal androgen receptor in prostate cancer development and progression, Cancers 9 (1) (2017) http://dx.doi.org/10.3390/cancers9010010.
[72] M. Guerrero, X.A. Li, Extending the linear–quadratic model for large fraction doses pertinent to stereotactic radiotherapy, Phys. Med. Biol. 49 (20) (2004) 4825, http://dx.doi.org/10.1088/0031-9155/49/20/012.
[73] C. Chargari, E.V. Limbergen, U. Mahantshetty, Deutsch, C. Haie-Méder, Radiobiology of brachytherapy: The historical view based on linear quadratic model and perspectives for optimization, Cancer/ Radiothérapie 22 (2018) 312–318, http://dx.doi.org/10.1016/j.canrad.2017.11.011.
[74] S.M. Bentzen, Preventing or reducing late side effects of radiation therapy: radiobiology meets molecular pathology, Nat. Rev. Cancer 6 (9) (2006) 702–713, http://dx.doi.org/10.1038/nrc1950.
[75] B. Djavan, A. Zlotta, C. Kratzik, M. Remzi, C. Seitz, C.C. Schulman, M. Marberger, PSA, PSA density, PSA density of transition zone, free/total PSA ratio, and PSA velocity for early detection of prostate cancer in men with serum PSA 2.5 to 4.0 ng/mL, Urology 54 (1999) 517–522, http://dx.doi.org/10.1016/s0090-4295(99)00153-3.
[76] R.G. Uzzo, N.B. Haas, P.L. Crispen, V.M. Kolenko, Mechanisms of apoptosis resistance and treatment strategies to overcome them in hormone-refractory prostate cancer, Cancer: Interdiscip. Int. J. Am. Cancer Soc. 112 (8) (2008) 1660–1671, http://dx.doi.org/10.1002/cncr.23318.
[77] I.A. Cetin, S.U. Akay, M. Sengoz, Prostate-specific antigen nadir within 1 year of radiotherapy combined with hormone therapy predicts cancer-specific mortality and biochemical recurrence-free survival in prostate cancer patients, BMC Urol. 22 (1) (2022) 182, http://dx.doi.org/10.1186/s12894-022-01125-1.
[78] F.B. Geara, M. Bulbul, R.B. Khauli, T.Y. Andraos, M. Abboud, A. Al Mousa, N. Sarhan, A. Salem, H. Ghatasheh, A. Alnsour, Z. Ayoub, I.A. Gheida, M. Charafeddine, M. Shahait, A. Shamseddine, R.A. Gheida, J. Khader, Nadir PSA is a strong predictor of treatment outcome in intermediate and high risk localized prostate cancer patients treated by definitive external beam radiotherapy and androgen deprivation, Radiat. Oncol. 12 (1) (2017) 149, http://dx.doi.org/10.1186/s13014-017-0884-y.
[79] C. Schuchardt, J. Zhang, H.R. Kulkarni, X. Chen, D. Müller, R.P. Baum, Prostate-specific membrane antigen radioligand therapy using 177Lu-PSMA I&T and 177Lu-PSMA-617 in patients with metastatic castration-resistant prostate cancer: Comparison of safety, biodistribution, and dosimetry, J. Nucl. Med. 63 (8) (2022) 1199–1207, http://dx.doi.org/10.2967/jnumed.121.262713.
[80] H.V. Jain, I.C. Sorribes, S.K. Handelman, J. Barnaby, T.L. Jackson, Standing variations modeling captures inter-individual heterogeneity in a deterministic model of prostate cancer response to combination therapy, Cancers 13 (8) (2021) http://dx.doi.org/10.3390/cancers13081872.
[81] J. Morote, A. Borque-Fernando, M. Triquell, A. Celma, L. Regis, R. Mast, I.M. de Torres, M.E. Semidey, A. Santamaría, J. Planas, L.M. Esteban, E. Trilla, Multiparametric magnetic resonance imaging grades the aggressiveness of prostate cancer, Cancers 14 (7) (2022) http://dx.doi.org/10.3390/cancers14071828.
[82] M. Ahdoot, A.H. Lebastchi, L. Long, A.R. Wilbur, P.T. Gomella, S. Mehralivand, M.A. Daneshvar, N.K. Yerram, L.P. O'Connor, A.Z. Wang, S. Gurram, J. Bloom, M.M. Siddiqui, W.M. Linehan, M. Merino, P.L. Choyke, P. Pinsky, H. Parnes, J.H. Shih, B. Turkbey, B.J. Wood, P.A. Pinto, Using prostate imaging-reporting and data system (PI-RADS) scores to select an optimal prostate biopsy method: A secondary analysis of the trio study, Eur. Urol. Oncol. 5 (2) (2022) 176–186, http://dx.doi.org/10.1016/j.euo.2021.03.004.
[83] M. Miszczyk, J. Rembak-Szynkiewicz, L. Magrowski, K. Stawiski, A. Namyśl-Kaletka, A. Napieralska, M. Kraszkiewicz, G. Woźniak, M. Stąpór-Fudzińska, G. Głowacki, B. Pradere, E. Laukhtina, P. Rajwa, W. Majewski, The prognostic value of PI-RADS score in CyberKnife ultra-hypofractionated radiotherapy for localized prostate cancer, Cancers 14 (7) (2022) 1613, http://dx.doi.org/10.3390/cancers14071613.
[84] CHAIMELEON Consortium, CHAIMELEON: Accelerating cancer research through AI and medical imaging, 2020, http://dx.doi.org/10.3030/952172.
[85] ProCAncer-I Consortium, ProCAncer-I: A platform for AI in prostate cancer imaging, 2020, http://dx.doi.org/10.3030/952159.
[86] ProCanAid consortium, ProCanAid: Gemelo digital para la detección, el diagnóstico asistidos del cáncer de próstata y la simulación de los efectos y la eficacia de diferentes tratamientos oncológicos, 2023.